NASA Langley FUN3D Analyses in Support of the 1st AIAA Stability and Control Prediction Workshop

Brett R. Hiller[1] and Michael D. Bozeman[2]
NASA Langley Research Center, Hampton, VA, 23681

This work summarizes the results of FUN3D analyses conducted for the 1st AIAA Stability and Control Workshop on behalf of participants from the NASA Langley Research Center. The workshop was created to establish best practices for the prediction of stability and control derivatives using computational fluid dynamics and assess the limitations of these methods when those best practices are applied. The inaugural workshop considered the ONERA version of the NASA/Boeing Common Research Model, which includes the wing, body, horizontal tail, and a vertical tail designed by ONERA. Wind tunnel data at small sideslip angles remain unpublished and served as 'blind' data for computational comparisons. The present research generated workshop test case data using the NASA FUN3D code, which is a parallelized, unstructured, node-based, finite-volume discretization, Reynolds-averaged Navier-Stokes flow solver. Steady-state numerical simulations were conducted for workshop test cases investigating the following: grid convergence, Mach number effect on static stability, wind tunnel sting increments, static stability-derivative calculations, and a sideslip angle sweep. Results were generated for two series of unstructured, mixed-element grids, one set provided by the workshop and another set created using the HeldenMesh™ grid generation software. The results provided include total- and component-level breakdowns of the force and moment coefficients, in addition to sectional pressure distributions for the wing and tail components for comparisons to wind tunnel data.

Nomenclature

Acronyms

CFD	=	Computational Fluid Dynamics
CFL	=	Courant-Friedrichs-Lewy
CRM	=	Common Research Model
DES	=	Delayed-Eddy Simulation
DPW	=	Drag Prediction Workshop
FUS	=	Fuselage
LRM	=	Large Reference Model
MAC	=	Mean Aerodynamic Chord
MRP	=	Moment Reference Point
NASA	=	National Aeronautics and Space Administration
ONERA	=	Office National d'Etudes et de Recherches Aérospatiales (French Aeronautics and Space Research Center)
QCR	=	Quadratic Constitutive Relationship
PWNG	=	Port Wing
RANS	=	Reynolds-averaged Navier-Stokes
SA	=	Spalart-Allmaras
SC	=	Stability and Control
SCPW01	=	1st AIAA Stability and Control Prediction Workshop
SWNG	=	Starboard Wing
TAIL	=	Horizontal and Vertical Tails
TOT	=	Total Configuration

[1]Research Aerospace Engineer, NASA Langley Research Center, Mail Stop 499, Hampton, VA 23681, AIAA Member.
[2]Research Aerospace Engineer, NASA Langley Research Center, Mail Stop 499, Hampton, VA 23681, AIAA Member.

Symbols

b_{ref}	=	Reference span, inches
S_{ref}	=	Reference area, square inches
T_{ref}	=	Reference temperature, degrees Fahrenheit
M	=	Mach number
Re_{MAC}	=	Reynolds number based on Mean Aerodynamic Chord
C_L	=	Lift coefficient
C_D	=	Drag coefficient
C_Y	=	Sideforce coefficient
C_m	=	Pitching moment coefficient
C_l	=	Rolling moment coefficient
C_n	=	Yawing moment coefficient
C_P	=	Pressure coefficient
α	=	Angle of attack, degrees
β	=	Angle of sideslip, degrees
δ	=	Boundary layer thickness, inches
η	=	Spanwise location
r_{FAC}	=	HeldenMesh™ grid source refinement factor
r_1, r_2	=	HeldenMesh™ boundary-layer stretch factors
N	=	Number of computational grid nodes
y^+	=	Inner scaling for wall-normal direction

I. Introduction

The 1st AIAA Stability and Control Prediction Workshop (SCPW01) was held virtually at the 2021 AIAA SciTech Conference. Based on the success of the Drag Prediction Workshop (DPW) [1], the SCPW workshop was motivated to establish the best practices for a specialized topic of interest in the prediction of Stability and Control (S&C) derivatives with Reynolds-averaged Navier-Stokes (RANS)- or Delayed Eddy Simulation (DES)-based Computational Fluid Dynamics (CFD) solvers and to assess the limitations of these methods when best practices are applied. The first workshop considered the ONERA version of the NASA/Boeing Common Research Model (CRM) [2, 3], which includes the wing, body, horizontal tail, and a vertical tail designed by ONERA, Office National d'Etudes et de Recherches Aérospatiales (French Aeronautics and Space Research Center). While longitudinal wind tunnel test data had already been previously published, unpublished data at small sideslip angles provided an opportunity for workshop participants to evaluate the effectiveness of various modeling and grid generation strategies in an impartial forum.

Participants were provided a 'family' of unstructured grids for the full-span ONERA CRM model with the wind tunnel sting included. This family of mixed-element grids consists of 5 levels of refinement (tiny, coarse, medium, fine, and extra fine) with surface and volume mesh scaling, resulting in a size range of 15 to 53 million nodes. A medium refinement mesh was also provided for the ONERA CRM configuration without a sting to evaluate the impact of the sting on static longitudinal stability characteristics. In addition to the workshop grids, the present work also considers an equivalent 'family' of computational grids generated using HeldenMesh™ [4], a rapid grid generation software by Helden Aerospace Corporation. These additional grids were generated to better understand the implications of using volume-mirrored grids for stability and control predictions after observing asymmetries in the workshop grids.

For the present work, test case data were generated using the NASA FUN3D code [5], which is a parallelized, unstructured, node-based, finite-volume discretization, RANS flow solver. Data are provided for the three primary workshop test cases, which include a grid convergence study, an assessment of the Mach number effect on static stability, and quantifying wind tunnel sting increments on longitudinal static stability. Additionally, data are provided for two optional test cases, which include static stability derivative calculations and a sideslip angle sweep. In each of the test cases, the vehicle is stationary, and the body is assumed to be rigid, where vehicle deformation has been accounted for in the model geometry. For all test cases, longitudinal and lateral force and moment aerodynamic coefficients are provided for the total configuration, in addition to a component-level breakdown that includes the port wing, starboard wing, fuselage, and tail, and surface pressure distribution slices along the wing and horizontal tail components.

II. Geometry

The workshop configuration, depicted in Fig. 1, is the ONERA Large Reference Model (LRM), which is a 1/16.835 scale CRM model that has been tested in the ONERA-S1MA wind tunnel. The geometry is the same as that used in the 6th AIAA Drag Prediction Workshop [2] with the addition of a horizontal tail from the 4th AIAA Drag Prediction Workshop [6] and an ONERA-designed vertical tail. Engine nacelles were removed, and the computational model was consistent with the flexible wing deflection at an angle of attack of 2.75 degrees. The Mean Aerodynamic Chord (MAC), wingspan (b_{ref}), reference area (S_{ref}), and Moment Reference Point (MRP) quantities for the configuration are listed in Table 1. Grids were generated with and without the sting to investigate its impact on static stability derivatives, for which all forces and moments were integrated about the LRM configuration with no sting included.

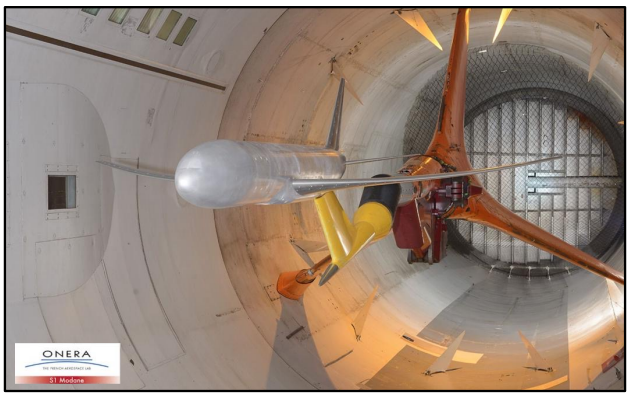

Figure 1. ONERA Large Reference Model (LRM) configuration.

Table 1. ONERA LRM configuration reference quantities.

MAC (in)	b_{ref} (in)	S_{ref} (in^2)	MRP (in)
16.38	137.42	2098.39	(x, y, z) = (78.76, 0.0, 10.57)

III. Test Cases

The SCPW workshop asked participants to submit data for four primary test cases and two optional test cases. The first of the primary test cases consisted of a 2D code verification study for CFD solvers not used in previous workshops, such as DPW. In the present work, the FUN3D flow solver was used and because of its widespread use, was not subject to the verification study. The remaining primary test cases consisted of investigations related to grid convergence, Mach number effects on static stability, and wind tunnel sting increments. The two optional test cases were a general stability derivative calculation study, for which participants were free to implement their best practices, and a sideslip angle sweep. Additionally, participants were invited to explore alternative flow solver approaches and user-generated grids.

For all of the test case descriptions below, the following attributes apply:

- Reynolds number is based on the wing MAC and freestream air speed
- Forces and moments are reported in the stability axis system
- For grids that included the sting, force and moment integration is computed using the configuration surfaces
- Reported forces and moments included the total configuration (TOT - fuselage, wings, tail), port wing (PWNG), starboard wing (SWNG), fuselage (FUS), and tail (TAIL - horizontal and vertical tail components)

A. Case 2 - Grid Convergence Study

Participants were asked to calculate the drag, side force, pitching moment, yawing moment, and rolling moment coefficients for the LRM with the wind tunnel mounting sting. The flow conditions were $\beta = 1°$, $M = 0.83$, $Re_{MAC} =$ 4.56 million, $C_L =$ 0.5 +/- 0.0001, and $T_{ref} = 100$ °F. The angle of attack should be approximately 2.94 degrees based on wind tunnel data. At a minimum, solutions should be generated for the coarse, medium, and fine grid refinement levels to assess grid convergence.

B. Case 3 - Mach Effect on Static Stability

To quantify the impact of Mach number on static stability, participants were asked to calculate the drag, side force, pitching moment, yawing moment, and rolling moment coefficients using the medium refinement grid for the LRM with the sting. The flow conditions were $\beta = 1°$, M = [0.7019, 0.8325, 0.8530, 0.8749, 0.9050], Re_{MAC} = [4.24, 4.56, 4.60, 4.62, 4.7] million, respectively, C_L = 0.5 +/- 0.0001, and T_{ref} = 100 °F. The angle of attack should be approximately 3.59, 2.94, 2.87 and 3.63 degrees, respectively, based on wind tunnel data. Due to symmetry, the moments at $\beta = 1°$ are also the derivative (per degree) calculated using a central difference scheme.

C. Case 4 - Wind Tunnel Sting Increments

Next, simulations were conducted to calculate the static longitudinal stability increment due to the sting for the LRM by performing simulations with and without the tunnel mounting sting using the medium refinement grids. The flow conditions of interest were $\beta = 0°$, $M = 0.83$, $Re_{MAC} = 4.56$ million, and T_{ref} = 100 °F. Simulations were conducted for C_L values of 0.48 and 0.52 ± 0.0001 so that $\Delta C_m/\Delta C_L$ at $C_L = 0.5$ could be estimated. Solutions were also generated at fixed angles of attack of 2.9 and 3.0 degrees so that $\Delta C_m/\Delta C_L$ at $\alpha = 2.95°$ could be estimated.

D. Case 5 - Stability Derivative Calculation

The side force, rolling moment, and yawing moment derivatives at $\beta = 0°$ can be estimated from the $\beta = 1°$ results using a central difference scheme and assuming symmetry as mentioned in case 3. For case 5, instead of using a central difference scheme, participants were asked to use their best practices to calculate these derivatives using additional simulation data as necessary for the medium refinement grids. Flow conditions were $M = 0.83$, $Re_{MAC} = 4.56$ million, C_L = 0.5 +/- 0.0001, and T_{ref} = 100 °F. The angle of attack was estimated to be approximately 2.94 degrees based on wind tunnel data.

E. Case 6 - Sideslip Angle Sweep

Finally, participants were asked to calculate the drag, side force, pitching moment, yawing moment, and rolling moment coefficients for the LRM with the tunnel mounting sting at various sideslip angles using the medium refinement grid. The flow conditions were $\beta = [1°, 3°, 5°]$, $M = 0.83$, $Re_{MAC} = 4.56$ million, C_L = 0.5 +/- 0.0001, and T_{ref} = 100 °F. The angle of attack should be approximately 2.94 degrees based on wind tunnel data.

IV. Computational Method

In addition to the workshop-provided grids, the present work also considers an equivalent 'family' of computational grids generated using HeldenMesh™. These custom grids were generated as a comparison to the workshop-provided grids that did not use mirrored grid volumes to better understand its impact on stability and control predictions. NASA FUN3D, a node-based RANS flow solver, was leveraged to perform steady-state, fully-turbulent solutions for each test case. The following section summarizes the HeldenMesh™ grid generation and FUN3D solution approaches. A detailed review of the workshop-provided grids can be found in the workshop summary paper [7].

A. HeldenMesh™ Grid Generation

A series of computational grids was generated using HeldenMesh™ v3.03 [4], a grid generation software system developed by Helden Aerospace Corporation for efficiently generating three-dimensional, mixed-element unstructured meshes of complex configurations. The HeldenMesh™ software consists of two tools, HeldenPatch™ and HeldenMesh™. HeldenPatch™ is the primary interface between the Initial Graphics Exchange Specification (IGES) geometry and the HeldenMesh™ grid generator that provides geometry clean-up, management, and transformation capabilities. The HeldenPatch™ software is capable of automatic surface patching to limit user-intervention. Prior to generating the grids in HeldenMesh™ GridTool was used to confirm that a water-tight geometry was created as desired by HeldenPatch™ and to specify user-defined patch names. GridTool is a geometry preprocessing tool contained in the TetrUSS software package [8] developed by the NASA Langley Research Center. HeldenMesh™ utilizes automated advancing-layers and advancing-front unstructured grid generation methods. A simple, text-based input file allows the user to control the spatial resolution of surface grid cells for each unique geometry component, as well as the viscous boundary layer growth rate and options for flow-feature resolution, e.g., wakes, shocks, etc., in the volume domain.

Mixed-element unstructured grids were generated for the LRM configuration with the sting to match the coarse, medium, and fine refinement levels, measured by grid nodes, of the workshop grids. These grids were generated after observing lateral grid asymmetries in the workshop grids to better assess any potential impact on the predicted lateral stability derivative values. In support of this objective, the HeldenMesh™ grids were generated by first creating a semispan grid and mirroring it about the configuration symmetry plane. Characteristics of the workshop and HeldenMesh™ grids are detailed in Tables 2 and 3, respectively. The workshop grid refinement levels ranged from 20.3 million nodes for the coarse grid to 39.5 million nodes for the fine grid. The HeldenMesh™ grids were created to produce grids of comparable resolution, ranging from 21.1 to 39.6 million total nodes, for participants using node-based CFD solvers. Differences in the number of cells may be attributed to differences in viscous cell types, for which the workshop grids predominantly used hexahedral elements in the boundary layer, whereas the HeldenMesh™ grids used prismatic cells.

Table 2. Characteristics of workshop grids.

Grid	Growth Rate	δ_1 [in]	Cells [million]	Nodes [million]
Coarse	1.172	1.16E-04	27.8	**20.3**
Medium	1.148	1.00E-04	38.1	**28.3**
Fine	1.127	8.75E-05	52.0	**39.5**

Table 3. Characteristics of HeldenMesh™ grids.

Grid	r_{FAC}	r_1	r_2	δ_1 [in]	Tets [million]	Pyramids [million]	Prisms [million]	Cells [million]	Nodes [million]
Coarse	1.08	0.181	0.015	1.14E-04	24.7	0.2	33.0	57.9	**21.1**
Medium	0.90	0.140	0.015	9.54E-05	22.2	0.3	49.8	72.2	**29.1**
Fine	0.68	0.082	0.015	7.16E-05	18.6	0.3	71.7	90.6	**39.6**

The HeldenMesh™ grid generation approach began with development of the coarse grid by setting the near-wall, first-node spacing (δ_1) to match the initial spacing used in the coarse workshop grid. Beyond the first layer of prism cells, the advancing layers (i) grow into the volume domain based on a two-variable stretching factor (r_1 and r_2) equation as defined by Eq. 1. The minimum surface spacing, nominal surface spacing, maximum stretching ratio, and maximum facet curvature angle were uniquely set for each vehicle component. For the baseline coarse grid, the fuselage and sting were prescribed to have nominal and minimum surface spacings of 5 in. and 0.025 in., respectively. The wing, horizontal tail, vertical tail, and strut all had identical grid resolution with a nominal spacing of 1 in. and a minimum surface spacing of 0.005 in. The trailing edges of the wing and tail components were set to achieve approximately 5 node layers across each surface. For each geometry component, the maximum facet curvature angle was set to 3 degrees to better resolve highly curved surface areas subject to the minimum surface spacing constraint. The maximum cell stretching ratio was set to 10 for the fuselage and sting and 7.5 for the wing, tail, and strut components. Increased cell stretching on the fuselage and sting allows for a larger proportion of the total grid nodes to be created on the lifting wing and tail surface that are more critical for CFD aerodynamic predictions.

$$\delta_{i+1} = \delta_i \cdot [1 + r_1 \cdot (1 + r_2)^i]^i \tag{1}$$

To generate the higher grid refinements, a global refinement factor, r_{FAC}, within HeldenMesh™ was used to linearly scale the spatial resolution of the grid surface cells and the viscous volume domain normal to the configuration surface. A NASA internal boundary layer refinement tool was used to calculate the boundary layer growth stretch factors, such that the total boundary layer height could be maintained across each level of grid refinement while changing the boundary layer resolution. The refinement and boundary layer stretch factors were iteratively changed until the target number of grid nodes was reached for each level of refinement.

Examples of the resulting surface grid resolution for the workshop (left) and HeldenMesh™ (right) grids at the medium refinement level are shown in Fig. 2. Figures 2(a) and 2(b) show a top view of the LRM configuration, while Figs. 2(c) and 2(d) show a perspective view of the full configuration with the wind tunnel mounting sting. While the node count between the two grids are approximately the same, it is evident that the surface curvature constraint within HeldenMesh™ more finely resolves the leading- and trailing-edges of the wing and tail components, in addition to highly curved surfaces, such as the nose of the fuselage and end of the sting. By specificying a greater cell-stretching ratio for the fuselage and sting, which are the less-critical lifting components, HeldenMesh™ is able to prioritize smaller nominal cell spacings on the wing and tail components.

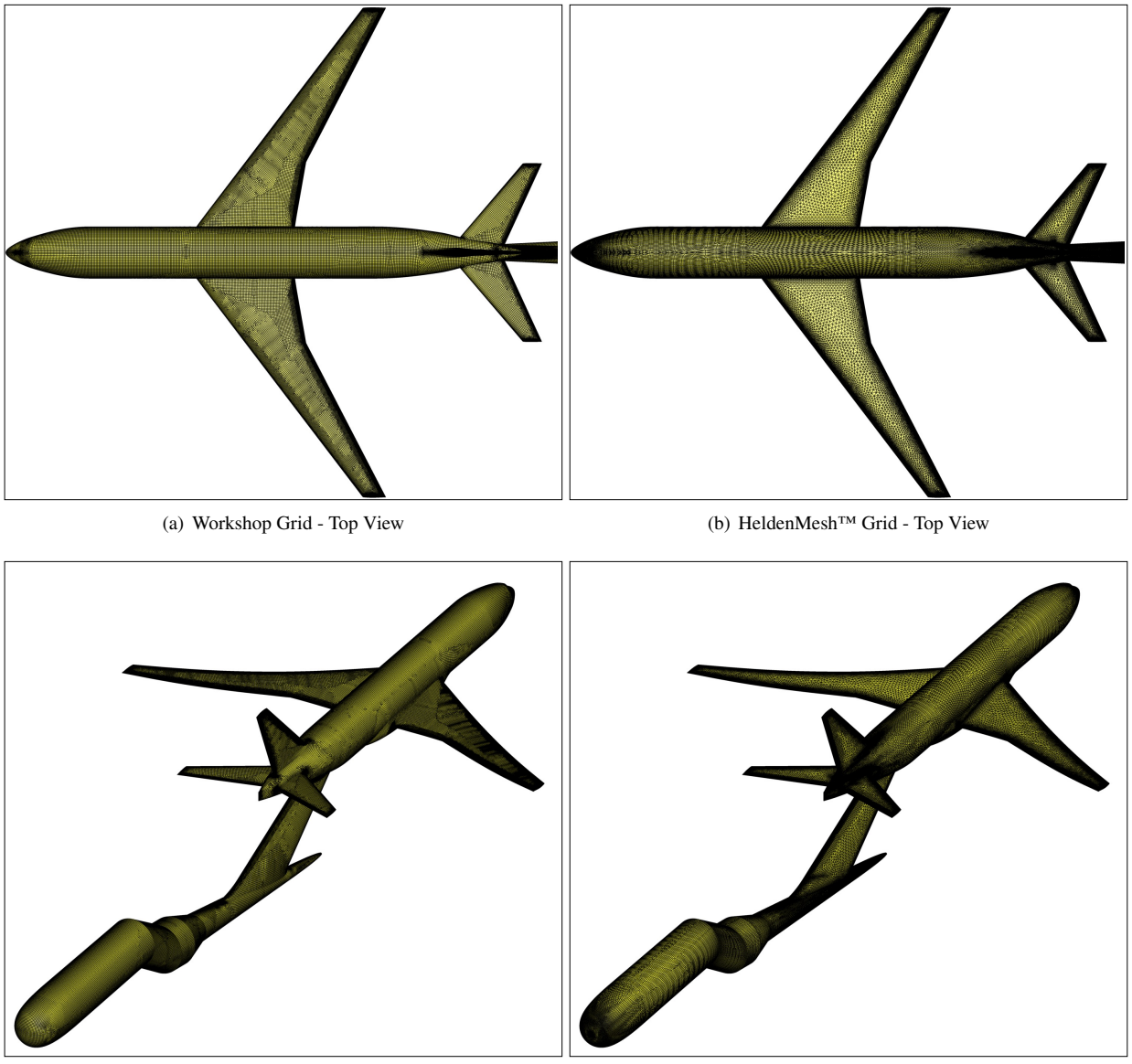

(a) Workshop Grid - Top View

(b) HeldenMesh™ Grid - Top View

(c) Workshop Grid - Perspective View

(d) HeldenMesh™ Grid - Perspective View

Figure 2. Surface grid resolution of medium workshop (left) and HeldenMesh™ (right) grids as shown from a top view (top) and perspective view (bottom).

Illustrations of the volume grid resolution for the workshop (left) and HeldenMesh™ (right) grids at the medium refinement level are shown in Fig. 3. Figures 3(a) and 3(b) show a symmetry-plane view, while Figs. 3(c) and 3(d) show a cross-sectional view located at the moment center of the configuration. The symmetry and sectional plane views confirm the asymmetry of the workshop grids and illustrate the volume-mirroring of the HeldenMesh™ grids. In the symmetry view, this is visualized by the cross-sectional cutting of volume cells for the workshop grids, while the HeldenMesh™ grid shows flat cell faces parallel to the symmetry plane about which it is mirrored. This asymmetry is also observed in the cross-sectional plane view about the configuration moment center, where the workshop grid shows lateral asymmetries in the boundary layer and inviscid volume domain that are not seen in the HeldenMesh™ grid. The impact of nonmirrored volume grids is evaluated in Test Case 5 when computing the lateral force and moment aerodynamic coefficients at various sideslip angles.

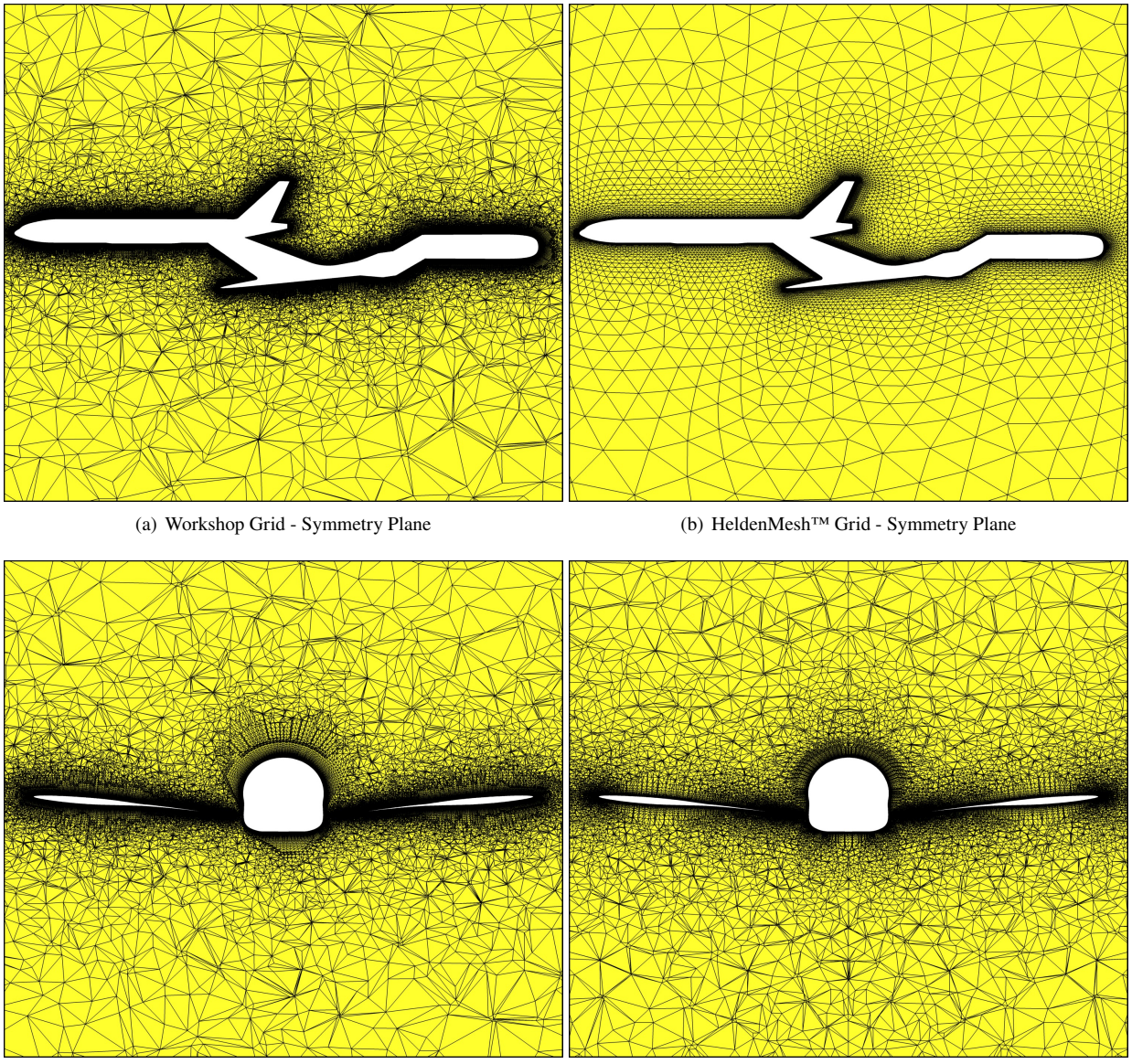

(a) Workshop Grid - Symmetry Plane

(b) HeldenMesh™ Grid - Symmetry Plane

(c) Workshop Grid - Sectional Plane

(d) HeldenMesh™ Grid - Sectional Plane

Figure 3. Volume grid resolution of medium workshop (left) and HeldenMesh™ (right) grids as shown from a symmetry plane view (top) and sectional view (bottom).

B. FUN3D Flow Solver

FUN3D v13.6 is a parallelized, unstructured, node-based, finite-volume discretization, RANS flow solver [5]. Inviscid flux quantities are computed using a variety of upwind flux functions. Turbulence models currently available include Spalart-Allmaras (SA), Menter k-omega Shear Stress Transport (SST), Wilcox k-omega, and detached eddy simulations, among others. In the present study, the standard SA turbulence model with negative provisions [9], a rotation/curvature (RC) correction [10], and the Quadratic Constitutive Relation (QCR) [11] was used. Inviscid fluxes were computed with Roe's flux-difference-splitting scheme [12] without limiting. The boundary conditions consisted of a surface no-slip condition on the configuration with farfield boundary conditions.

For all of the test case simulations, the solution was initialized with 1,000 first-order iterations with aggressive CFL (Courant-Friedrichs-Lewy) ramping from 1 to 250. Next, a restart simulation was submitted to achieve convergence at a fixed test case condition with second-order iterations and moderate CFL ramping from 1 to 100 to advance the meanflow and turbulence equations. For test cases in which the total lift coefficient was to be matched to wind tunnel data, a FUN3D internal lift-coefficient matching command-line-option was leveraged to automatically iterate on the configuration angle of attack until the desired lift coefficient was met. For this additional simulation, 5,000 second-order iterations were performed using a constant CFL of 100. In each test case, the solution strategy yielded lift coefficient convergence within a tolerance of +/- 0.0001.

V. Results

This section reviews the FUN3D results for each of the workshop test cases using both the workshop and HeldenMesh™ grids. For each test case, the relevant total and component aerodynamic force and moment coefficients are provided to better assess sources of prediction variability and to evaluate differences between the two grid series. ONERA wind tunnel measurements of the configuration total aerodynamic force and moment coefficients are provided for test cases 2 and 3, which investigate grid convergence at a small sideslip angle and the impact of Mach number on aerodynamic predictions, respectively. Additionally, for test case 3, FUN3D sectional pressure distribution results are provided for each grid series at select locations on the wing and horizontal tail components with comparisons to pressure data from the ONERA wind tunnel tests. For each test case, the CFD conditions were matched to those of the ONERA wind tunnel test, for which corrections were applied to account for wall, sting, and wind tunnel up-wash effects. A summary of the ONERA wind tunnel test conditions and measurements can be found in the workshop summary paper [7].

A. Case 2 - Grid Convergence

For Test Case 2, participants were tasked with computing the drag, side force, pitching moment, rolling moment, and yawing moment coefficients for the ONERA LRM configuration with the wind tunnel sting for the coarse, medium, and fine grid refinement levels to assess grid convergence at $M = 0.83$, $Re_{MAC} = 4.56$ million, $\beta = 1^\circ$, for a fixed $C_L = 0.5 \pm 0.0001$. Simulations were conducted at the noted conditions for both the workshop and HeldenMesh™ grid series. Figures 4-9 provide the total and component-level force and moment coefficients vs. grid factor, $1/N^{2/3}$, where N is the number of grid nodes, for each grid. Using the standard Richardson extrapolation method [13], grid refinement is considered converged when the computational solutions demonstrate asymptotic convergence vs. grid factor. This is observed when the solution decreases in error toward a monotonic fit with increased grid refinement. Extension of the solution fit to the y-intercept would then provide the theoretical computational solution for an infinitely-resolved grid at the simulated test condition. Assessments of the observed grid factor trends are noted along with comments on the component-level aerodynamic coefficient variability for the fuselage, port wing, starboard wing, and tail components.

Figure 4 shows the convergence of the total and component lift coefficients vs. grid factor. The total lift coefficient for each grid is successively matched to the target wind tunnel value of $C_L = 0.5 \pm 0.0001$. At the component level, the HeldenMesh™ grids show a more monotonic solution fit relative to the workshop grids, which show a nonmonotonic variation over the coarse, medium, and fine refinement levels. For the fuselage and tail (horizontal and vertical) components, the HeldenMesh™ grid predicts higher lift coefficient values compared to the workshop grids on the order of one lift count (0.001). Conversely, the lift coefficient for the port and starboard wings show that the workshop grids predict higher values relative to the HeldenMesh™ grids. While the total number of nodes are matched between the two grid series, it is important to note that due to the higher resolution of the highly curved geometry surfaces, such as the leading and trailing edges, the HeldenMesh™ grids had a larger average nominal spacing on the interior regions of each surface domain. This feature is a possible source leading to the small variability between this and other test case predictions for the two grids.

In Fig. 5, the variation of the total and component drag coefficients with grid factor is shown. While not showing a monotonic fit in the solution, the total drag coefficient for the workshop grids is in good agreement with the wind tunnel data as they predict a coefficient value within 1 to 2 drag counts (0.0001). The HeldenMesh™ grids are also observed to be in general agreement with the experiment, predicting a coefficient value within 5 to 6 drag counts. At the component level, the workshop and HeldenMesh™ grids show similar predictions for the fuselage with a difference near one drag count. For the wing and tail components, the workshop grid generally predict higher drag values relative to the HeldenMesh™ grids, which partially contributes to the underprediction. From a grid convergence perspective, the HeldenMesh™ grid shows a monotonic solution fit for each coefficient with the wing and tail components resolved within less than one drag count of error. The predicted fuselage drag coefficient appears to be monotonically decreasing with increased grid refinement, suggesting that perhaps the increased cell stretching on the fuselage component leads to inadequate spatial resolution relative to the other components. The workshop grids show a slightly nonmonotonic variation in the component drag coefficients that was reflected in the total drag coefficient. The convergence of side force coefficient vs. grid factor is shown in Fig. 6. Both the workshop and HeldenMesh™ grids agree well with each other and tend to overpredict the total side force coefficient relative to the wind tunnel data by approximately 7.5%. The component level coefficients show the same relative trends and variation in coefficient magnitude. These results suggest that the side force coefficient is less sensitive compared to the drag coefficient at small sideslip angles.

Figure 7 illustrates the convergence of total and component pitching moment coefficients relative to the wind tunnel data. The workshop and HeldenMesh™ grids predict a more negative (nose-down) pitching moment relative to the wind tunnel data, approximately 20% less than the experimental value. Between the two grid series, the HeldenMesh™ grid prediction is nearly 3% lower than the workshop grids with a monotonic solution fit, as seen with the other coefficients. The predicted pitching moment contribution from the fuselage compares favorably between the grids. On the wing components, the workshop grid predicts more aft loading relative to the HeldenMesh™ grids. For the tail, the HeldenMesh™ grid is observed to predict a reduced pitching moment nearly 12% less than the workshop grids. From a grid convergence perspective, both grids show a monotonic fit for each component coefficient, with the exception of the workshop-grid results for the tail. In any case, the total pitching moment coefficient extrapolated values are expected to be even further reduced relative to the wind tunnel data.

Figure 8 shows the FUN3D predictions for the total and component rolling moment coefficients vs. grid factor. The workshop and HeldenMesh™ grids are shown to be in close agreement with each other and within one count (0.0001) of the wind tunnel measurement of total rolling moment coefficient. On the component level, the fuselage and tail coefficient values show limited variation with grid factor for both grid series. In contrast, the port and starboard wing predictions show more pronounced, though limited, changes in rolling moment coefficient with grid refinement. The yawing moment coefficient convergence for the total configuration and its components is provided by Fig. 9. Similar to the rolling moment coefficient, the workshop and HeldenMesh™ grids are in close agreement, within one count of each other for every refinement level. Additionally, both grid series slightly underpredict the total rolling moment coefficient relative to the wind tunnel data by approximately two counts. The fuselage has a relatively low contribution to rolling moment coefficient and compares favorably between both grids. The port and starboard wings have nearly identical contributions (opposite in sign) in rolling moment at the small sideslip angle. The tail component represents the largest contribution to the total rolling moment coefficient and both grid series agree favorably and show an increasingly positive side force coefficient value with increasing grid refinement. This observation extends to the total rolling moment coefficient, for which the extrapolated solution values would agree more closely with the experimental data. Generally, the lateral moment coefficient predictions show favorable agreement relative to the wind tunnel results.

Overall, the FUN3D test case results showed general agreement between the predicted force and moment coefficients for both the workshop and HeldenMesh™ grid series with the exception of pitching moment, for which the solutions underpredicted the experimental values by approximately 20%. At the component level, the tail showed the most variability in pitching moment and represented the biggest source of discrepancy between the two grid series. These observations align with a general sentiment that pitching moment is the most challenging of the force and moment coefficients to predict with state-of-the-art RANS solvers. From a grid convergence perspective, the workshop grids consistently demonstrated a nonmonotonic variation in solution fit for each component coefficient relative to grid factor, suggesting predictions could benefit from increased grid resolution for the chosen gridding strategy. The HeldenMesh™ grids showed a more monotonic solution fit for most coefficients, a trend generally observed for HeldenMesh™ grids due to the uniform grid scaling for each refinement level based on the internal source scaling factor (r_{FAC}). While the subsequent test cases could potentially benefit from more refined grids, the medium refinement level was chosen to provide a more practical option for limiting computational resources and increasing the chances of complete workshop participation.

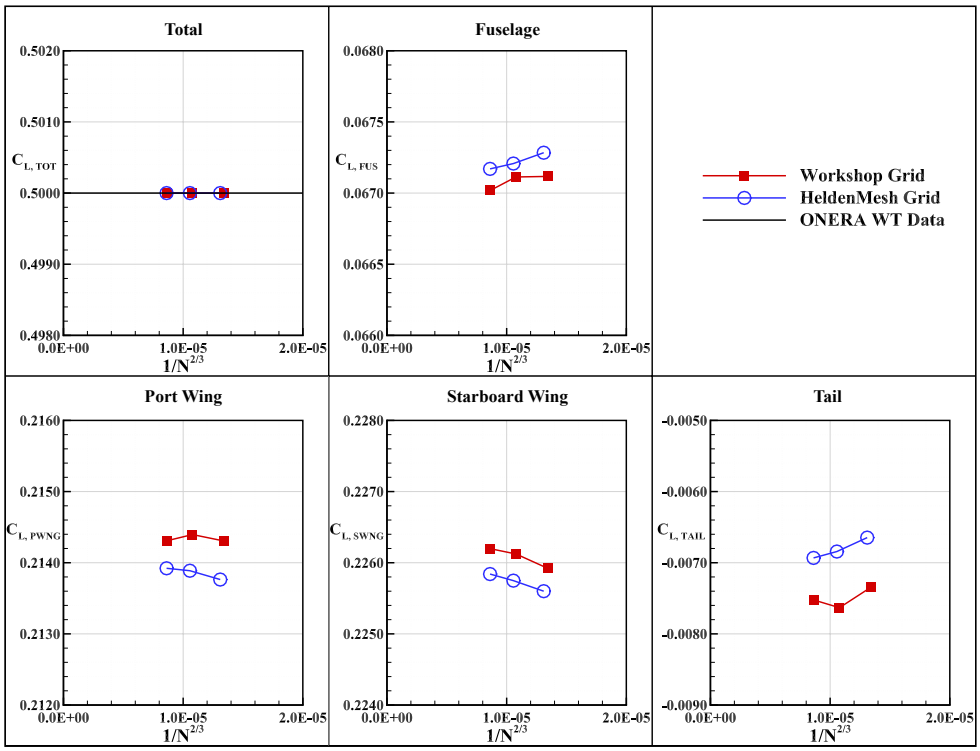

Figure 4. Convergence of total and component lift coefficients vs. grid factor (M = 0.83, C_L = 0.5).

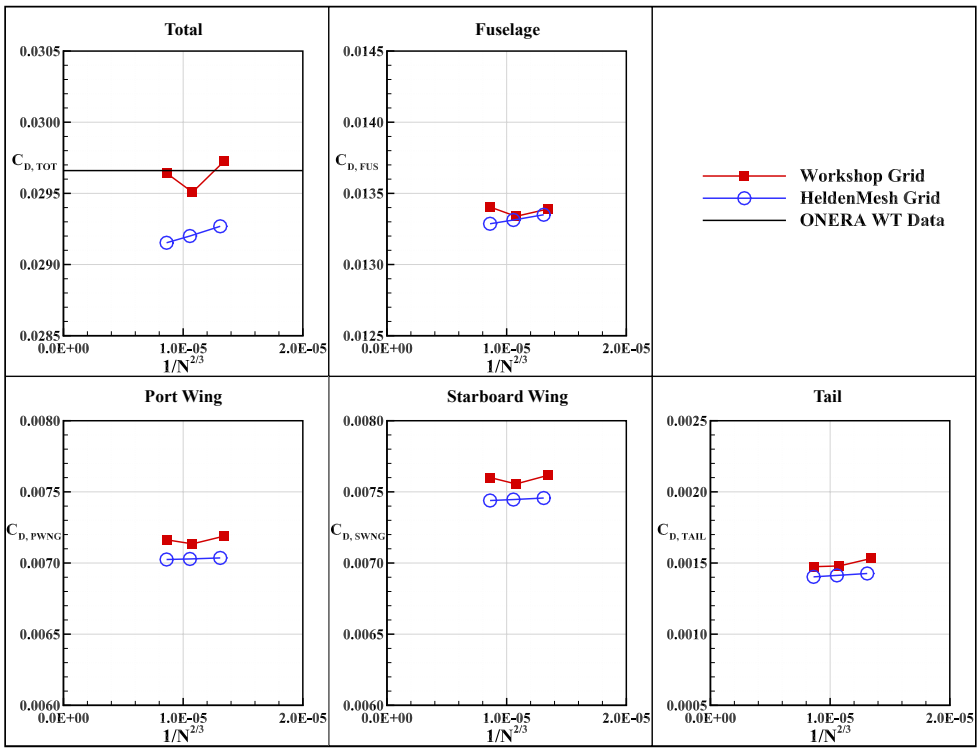

Figure 5. Convergence of total and component drag coefficients vs. grid factor (M = 0.83, C_L = 0.5).

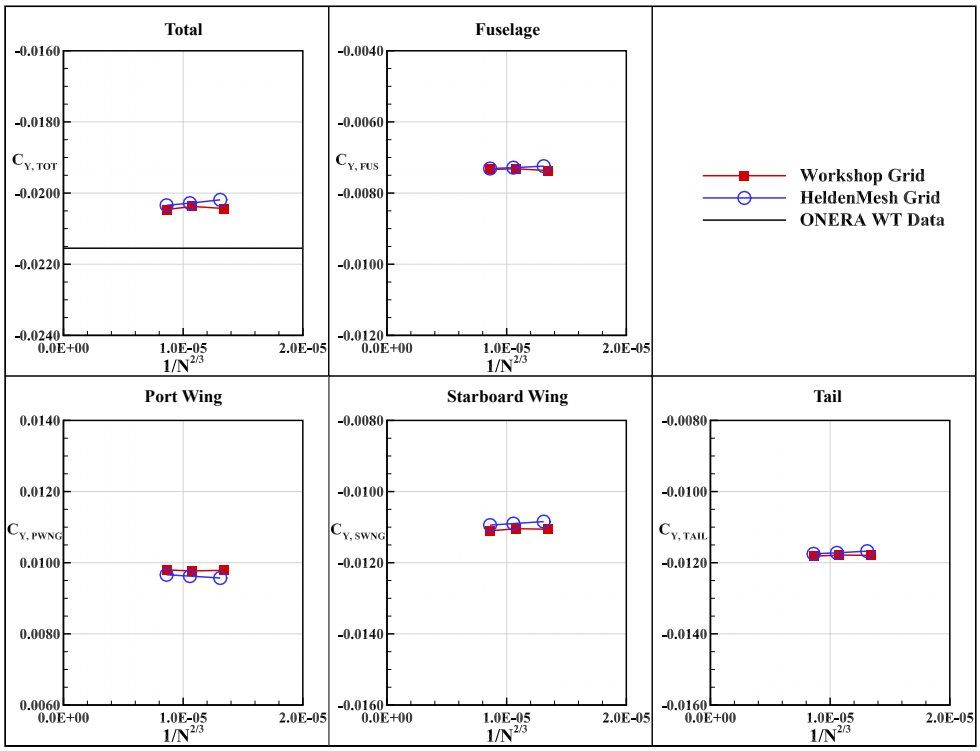

Figure 6. Convergence of total and component side force coefficients vs. grid factor (M = 0.83, C_L = 0.5).

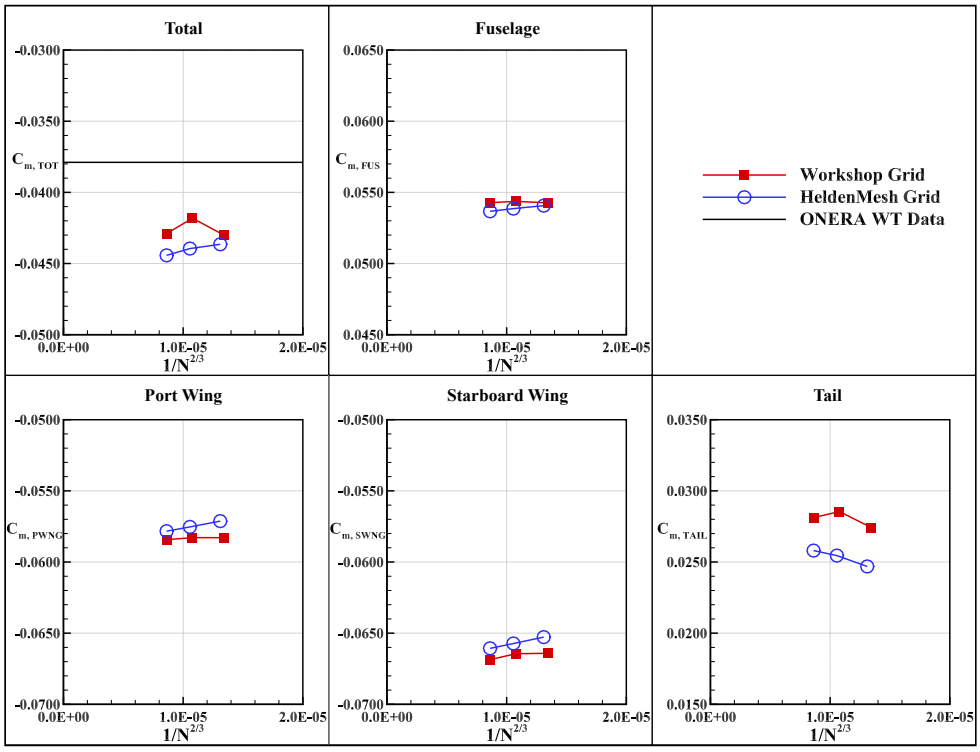

Figure 7. Convergence of total and component pitching moment coefficients vs. grid factor (M = 0.83, C_L = 0.5).

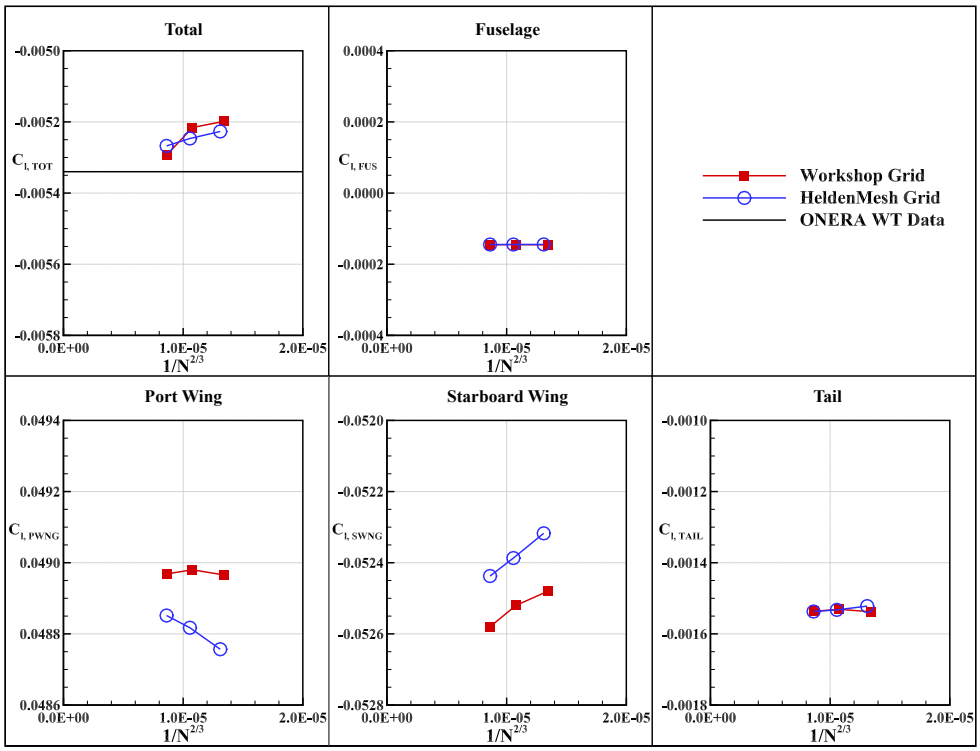

Figure 8. Convergence of total and component rolling moment coefficients vs. grid factor (M = 0.83, C_L = 0.5).

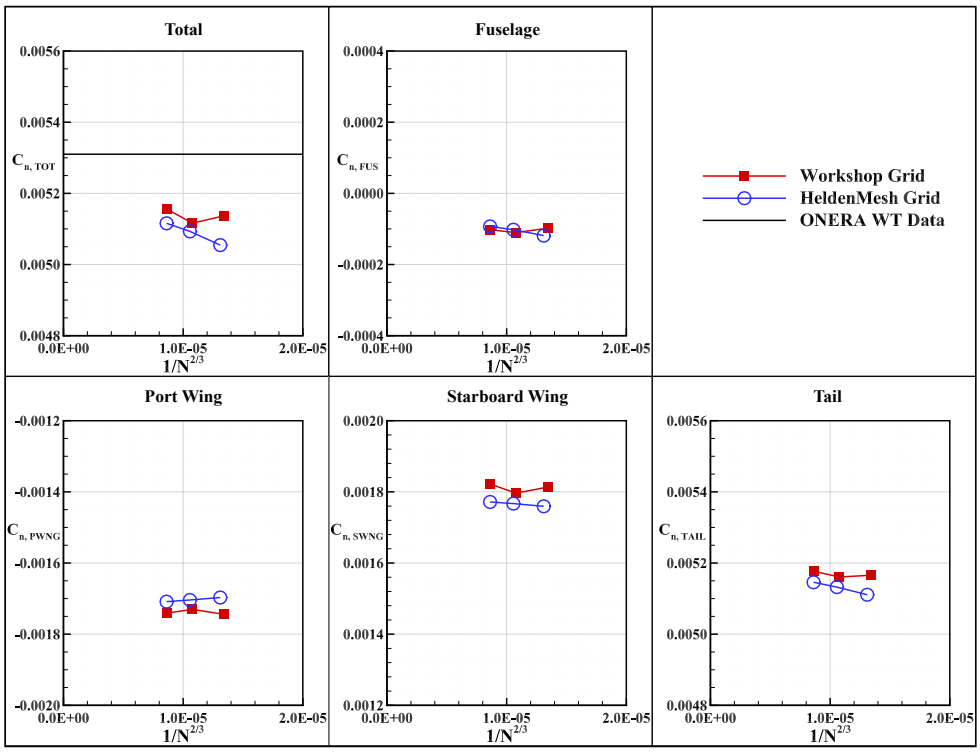

Figure 9. Convergence of total and component yawing moment coefficients vs. grid factor (M = 0.83, C_L = 0.5).

B. Case 3 - Mach Effect on Static Stability

Test case 3 focused on assessing the impact of Mach number on static stability by calculating the aerodynamic forces and moments using the medium refinement grid for the ONERA LRM configuration with the wind tunnel mounting sting included at various Mach numbers. FUN3D simulations were conducted for M = [0.7019, 0.8325, 0.8530, 0.8749, 0.9050] at a fixed C_L= 0.5 ± 0.0001 for comparisons to wind tunnel data. The angle of attack varied as needed to match the target lift coefficient, and the sideslip angle was set to $\beta = 1^\circ$. The following section provides total and component aerodynamic force and moment coefficient variations with Mach number, in addition to sectional pressure distribution comparisons to wind tunnel data at each Mach number.

Figure 10 shows the FUN3D predictions of the total aerodynamic force and moment coefficients for both the workshop and HeldenMesh™ grid series compared to the ONERA wind tunnel data measurements. The total lift coefficient matches well for the HeldenMesh™ grid, whereas the workshop grids encountered difficulties in reaching the target lift coefficient within FUN3D at Mach numbers above 0.87. The drag coefficient predictions for both sets of grids compare well with the wind tunnel data at lower Mach numbers, but generally underpredict the drag at Mach 0.90 by 50 to 60 drag counts, though matching the qualitative trend. For side force coefficient, the grids are observed to have a similar qualitative decrease with increases in Mach number from 0.70 to 0.85. However, the workshop and HeldenMesh™ grids overpredict the side force coefficient by approximately 5% in the lower Mach number range. At M = 0.87, the HeldenMesh™ grid agrees well with the experimental data, whereas the workshop grids show a strong nonlinear coefficient variation with a coefficient overpredicted by nearly 10%. This is likely to be attributed to the inability of the grids to reach the target lift coefficient at higher Mach numbers. At M = 0.90, the workshop grids show improved agreement with the wind tunnel data, despite a 5-count decrease in total lift coefficient from the match condition. For pitching moment, both grids underpredict the total coefficient value relative to the wind tunnel data from M = 0.70 to 0.85 by up to 8%. For M > 0.85, the workshop grid does well in predicting the pitching moment relative to the HeldenMesh™ grid, despite not matching the lift coefficient. At M = 0.90, the HeldenMesh™ grids predict a more negative pitching moment, which will be shown to be attributed to greater wing loading as a result of a more aft shock location. The rolling moment coefficient predictions from both grids correlate well with the wind tunnel data at every Mach number. Finally, the yawing moment coefficient predictions between the two grids are in general agreement with each other in the low Mach number range but underpredict the coefficient value measured in the wind tunnel. At M = 0.87, the HeldenMesh™ grid shows favorable agreement with the experimental data, whereas the workshop grids show poor agreement, likely due to the inability to match lift. At M = 0.90, the HeldenMesh™ grid retains good agreement with the wind tunnel data, while the workshop grids still deviate by overpredicting the yawing moment by approximately 10%. Overall, the FUN3D data suggest good qualitative agreement among the force and moment coefficient predictions with wind tunnel data at lower Mach numbers, with the pitching moment and side force coefficients showing the largest discrepancy, and general difficulties in predicting the high transonic aerodynamics.

Figure 11 provides a lift coefficient breakdown by component with variations in Mach number. Differences between the workshop and HeldenMesh™ grid are most prominent beyond M = 0.85, for which the workshop grids were unable to reach the target lift coefficient. The largest discrepancy arises at M = 0.90, where the workshop grids predict a higher lift coefficient on the starboard and port wings but a lower lift coefficient for the fuselage and tail components, relative to the HeldenMesh™ grids. The decreased lift on the fuselage and tail components is expected as the resulting configuration angle of attack was lower for the workshop grid. This also leads to increased lift on the wings due to decreased shock strength and flow separation associated with lower angles of attack at M = 0.90.

The variation of drag coefficient with Mach number is shown in Fig. 12. As reflected by the total drag coefficient, the component drag coefficient values agree favorably between the two grids and even the wind tunnel data with the exception of M = 0.90. At the highest Mach number, the predicted drag values are slightly higher for the workshop grids compared to the HeldenMesh™ grids. The results for side force coefficient provide similar observations in Fig. 13 with good correlation between the two grids at lower Mach numbers and slight variations at M = 0.90.

Figure 14 provides the pitching moment coefficient breakdown by component with variations in Mach number. The workshop and HeldenMesh™ grids show great agreement from M = 0.70 to 0.85 with larger discrepancies at the higher Mach numbers, where the mismatch in target lift coefficient translates to significiant differences in predicted pitching moment coefficient. These discrepancies are greater for the fuselage, and in particular, the tail component, for which the HeldenMesh™ grid predicts a reduced pitching moment, i.e., less aft loading on the tail (horizontal/vertical). The FUN3D results for rolling moment coefficient are shown in Fig. 15, which show good agreement between both grids and wind tunnel data. The most notable disagreement between the workshop and HeldenMesh™ grids arises in the predicted rolling moment contributions from the starboard and port wings. The yawing moment coefficient results in Fig. 16 further reinforce the discrepancy between the grids arising from disagreement in the predicted tail contribution.

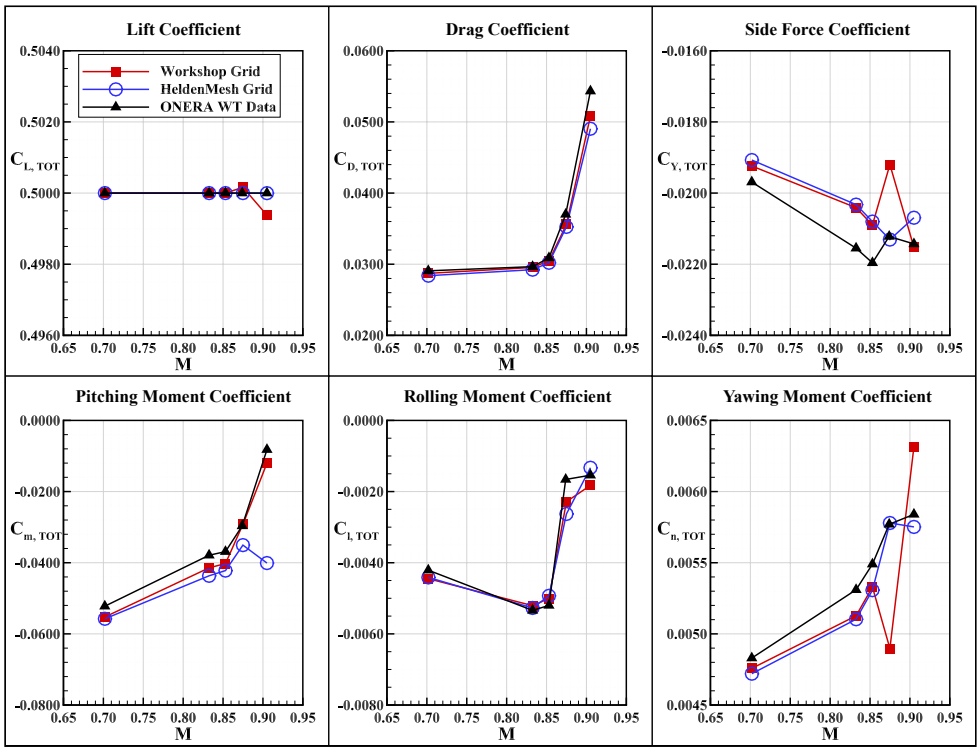

Figure 10. Total force and moment coefficients vs. Mach number (C_L = 0.5).

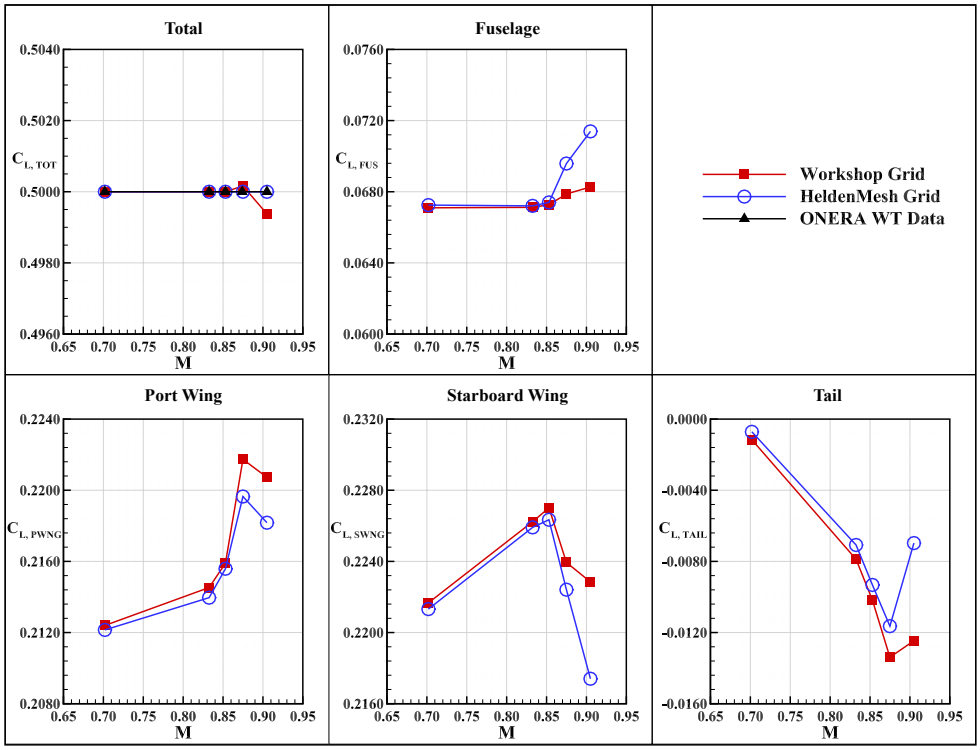

Figure 11. Total and component lift coefficients vs. Mach number (C_L = 0.5).

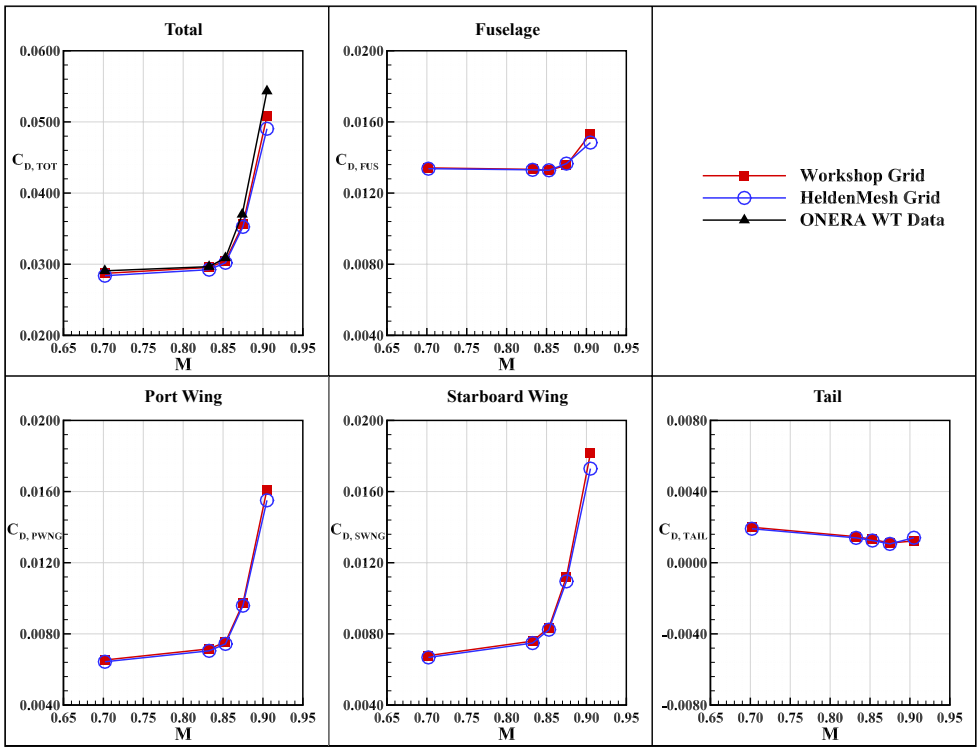

Figure 12. Total and component drag coefficients vs. Mach number (C_L = 0.5).

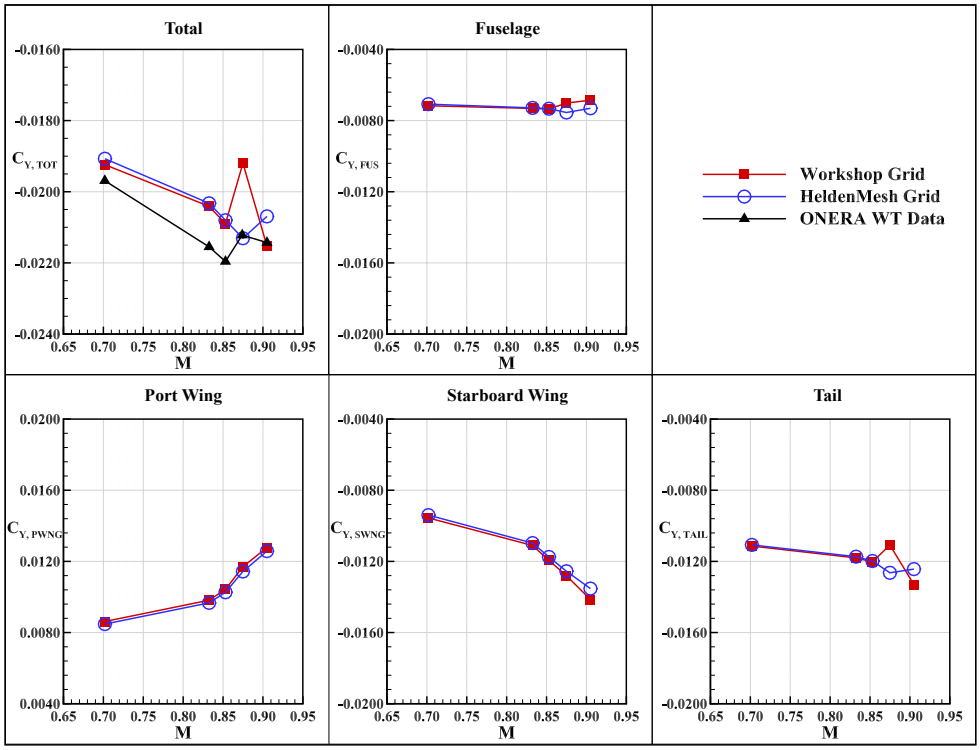

Figure 13. Total and component side force coefficients vs. Mach number (C_L = 0.5).

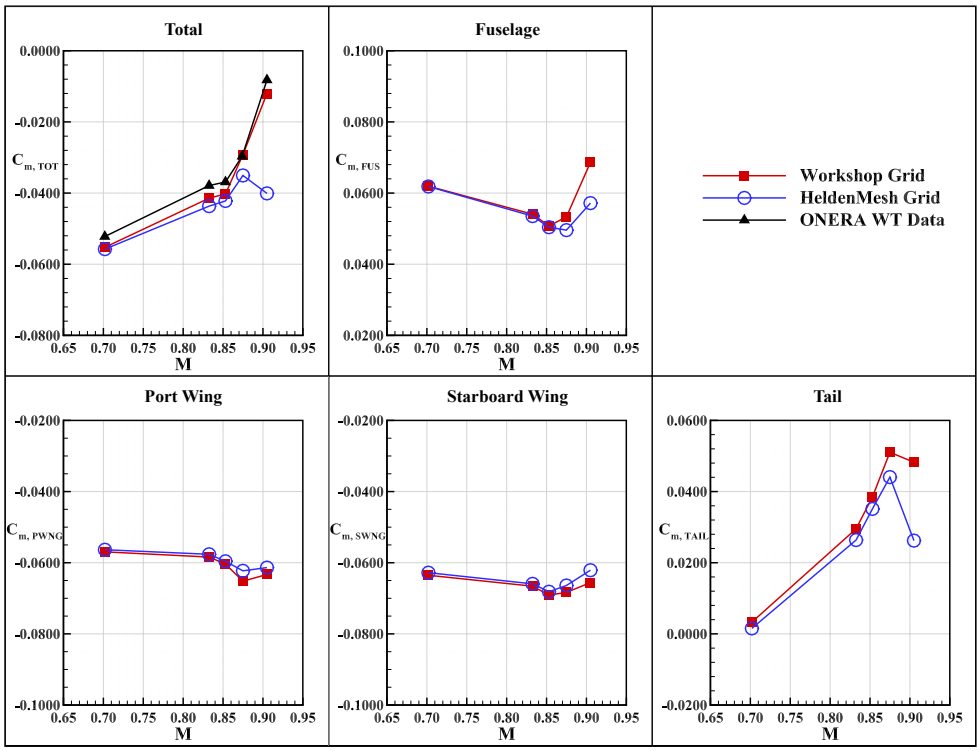

Figure 14. Total and component pitching moment coefficients vs. Mach number (C_L = 0.5).

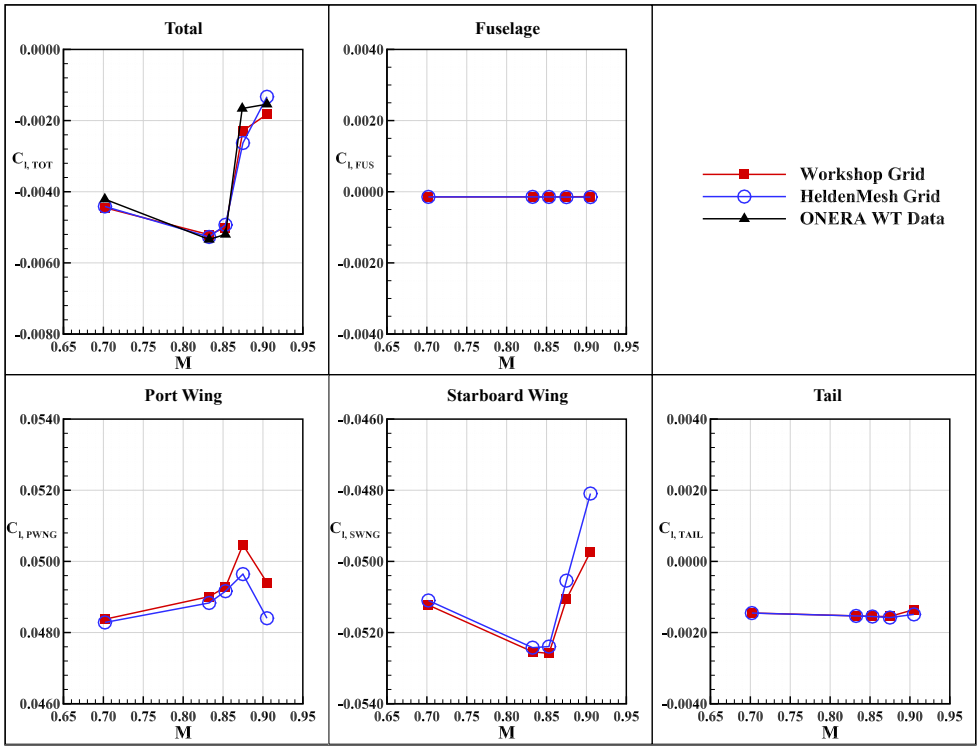

Figure 15. Total and component rolling moment coefficients vs. Mach number (C_L = 0.5).

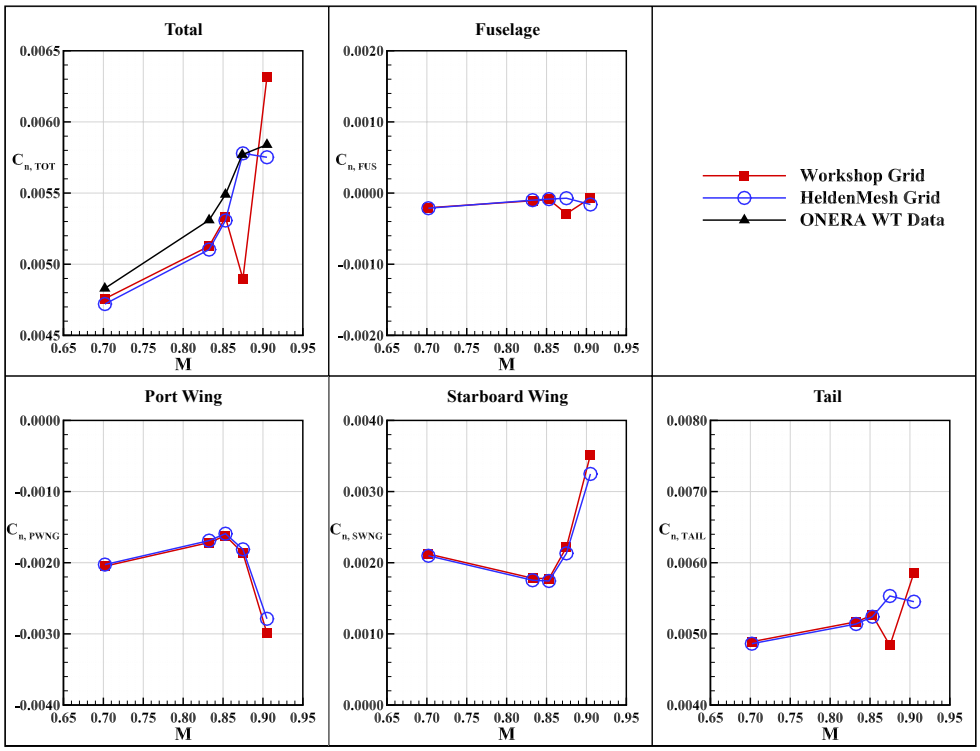

Figure 16. Total and component yawing moment coefficients vs. Mach numbe (C_L = 0.5).

In addition to the force and moment coefficient data decomposition, FUN3D sectional pressure distribution data for each grid were compared with measured experimental values at each Mach number. Five sectional cuts along the starboard wing, one sectional cut on the port wing, two sectional cuts on the starboard horizontal tail, and one sectional cut on the port horizontal tail are provided. For each Mach number, surface pressure contour data from the HeldenMesh™ grid solution is provided with the sectional slice stations [A through H] listed with their respective spanwise locations (η). The sections are alphabetically ordered with station A being near the wing-fuselage structure and station E near the wingtip. It is important to note that the corresponding experimental conditions do not exactly match the target lift coefficient. Two sets of wind tunnel data were available for lift coefficients slightly below and above the target lift coefficient of C_L = 0.5. Instead of interpolating the pressure data from two data sets, the surface pressure data corresponding to the slightly higher lift coefficient values is plotted versus the computational data for general assessments. The experimental Mach number and lift coefficient values are listed in Table 4.

Table 4. Experimental conditions for Test Case 3.

M	C_L
0.7019	0.510
0.8325	0.503
0.8530	0.513
0.8749	0.503
0.9050	0.508

Figure 17 shows the HeldenMesh™ pressure contour data at $M = 0.70$ with the noted sectional reference locations. The corresponding sectional pressure distributions for $M = 0.70$ are shown in Fig. 18. As might be expected due to the good agreement observed in the force and moment predictions, the pressure distribution data for both grids shows excellent agreement with the experimental wind tunnel data on the wing and tail components. Slight discrepancies between the CFD solutions and experimental data are observed in relation to the leading-edge acceleration at starboard wing stations B and C, as well as for the more outboard stations (G and H) on the horizontal tail. The pressure contour and sectional pressure distribution data at $M = 0.83$ are provided in Figs. 19 and 20, respectively. The surface pressure data shows greater leading-edge acceleration and a more aft pressure recovery due to the increased Mach number. Again, the computational results are shown to be in excellent agreement with the experimental data for each component and section. Slight variations between the two grids are observed at the midspan station [C] on the starboard wing with the HeldenMesh™ grid showing a smoother shock distribution. Figures 21 and 22 illustrate the pressure data comparisons at $M = 0.85$. At this higher Mach number, the midspan pressure distributions on the wing show an increase in lift production and a stronger, more aft shock. Both grid solutions show excellent agreement relative to the experimental data with the HeldenMesh™ solution showing smoother and more accurate pressure distribution variations in the vicinity of the shock.

As Mach number is increased into the higher transonic range, discrepancies between the grid solutions and experimental data become more prominent. The surface pressure contour data and sectional pressure distribution data for $M = 0.87$ are shown in Figs. 23 and 24, respectively. Near the wing-fuselage juncture, the HeldenMesh™ solution shows favorable agreement with the wind tunnel data, whereas the workshop grid shows a more forward shock location and more gradual pressure recovery. Moving outboard, both the workshop and HeldenMesh™ grids show a slightly more aft shock location relative to the experimental data with the HeldenMesh™ solution continuing to show a more physical variation in pressure near the shock. The surface and sectional pressure data at $M = 0.90$ is shown in Figs. 25 and 26. In this case, both grids predict a much further aft shock location for the most inboard wing station relative to wind tunnel data. At the inboard section B on the starboard wing, the computational solutions are in excellent agreement with the experiment. At the more outboard wing stations C and D, the experimental data suggests post-shock separation with a relatively zero pressure gradient. This separation feature is captured in each grid, though at a more aft chordwise location. Near the wingtip, the computational results show good agreement again with the experimental data. On the tail component, both grid solutions show difficulties in matching the leading-edge acceleration of the most inboard section [F]. However, the HeldenMesh™ grid compares more favorably and does better in predicting the midchord pressure variation. For the the more outboard tail sections, the HeldenMesh™ grid shows better agreement with the experimental data. This can at least be partially attributed to the inability to match the target lift coefficient for the workshop grids, for which the tail pressure distributions show the most variability relative to the HeldenMesh™ grids.

In summary, the FUN3D pressure distribution predictions for the workshop and HeldenMesh™ grids showed favorable agreement with the ONERA wind tunnel data across the lower Mach range of 0.70 to 0.85 with only minor variations in numerical shock shmearing. At the higher transonic Mach numbers, the grids show notable differences in predicted shock location on the port and starboard wings and an inability to match the pressure contributions on the horizontal tail component. Future workshops may consider the incorporation of grid adaptation methods, whereby flow-feature-based metrics, such as Mach number, may be used to better resolve the shock behavior on the wing and tail components. Additionally, the incorporation of volume sourcing in the vicinity of the wing and tail components could improve wake resolution to better capture component-level aerodynamic interactions.

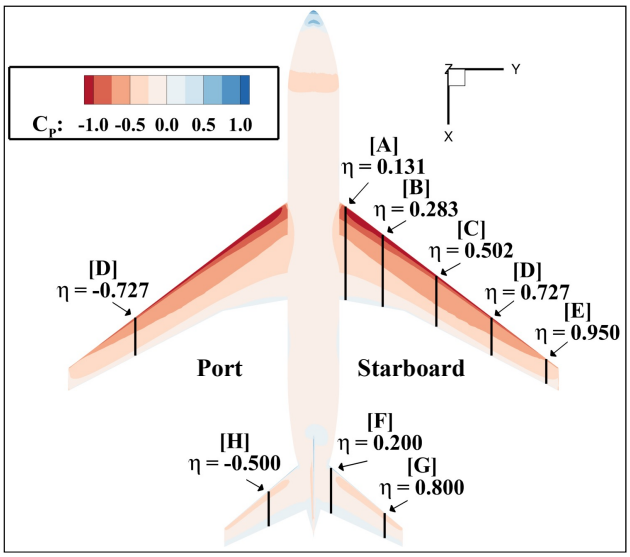

Figure 17. FUN3D pressure contours for medium refinement level of HeldenMesh™ grid at M = 0.70 (C_L = 0.5).

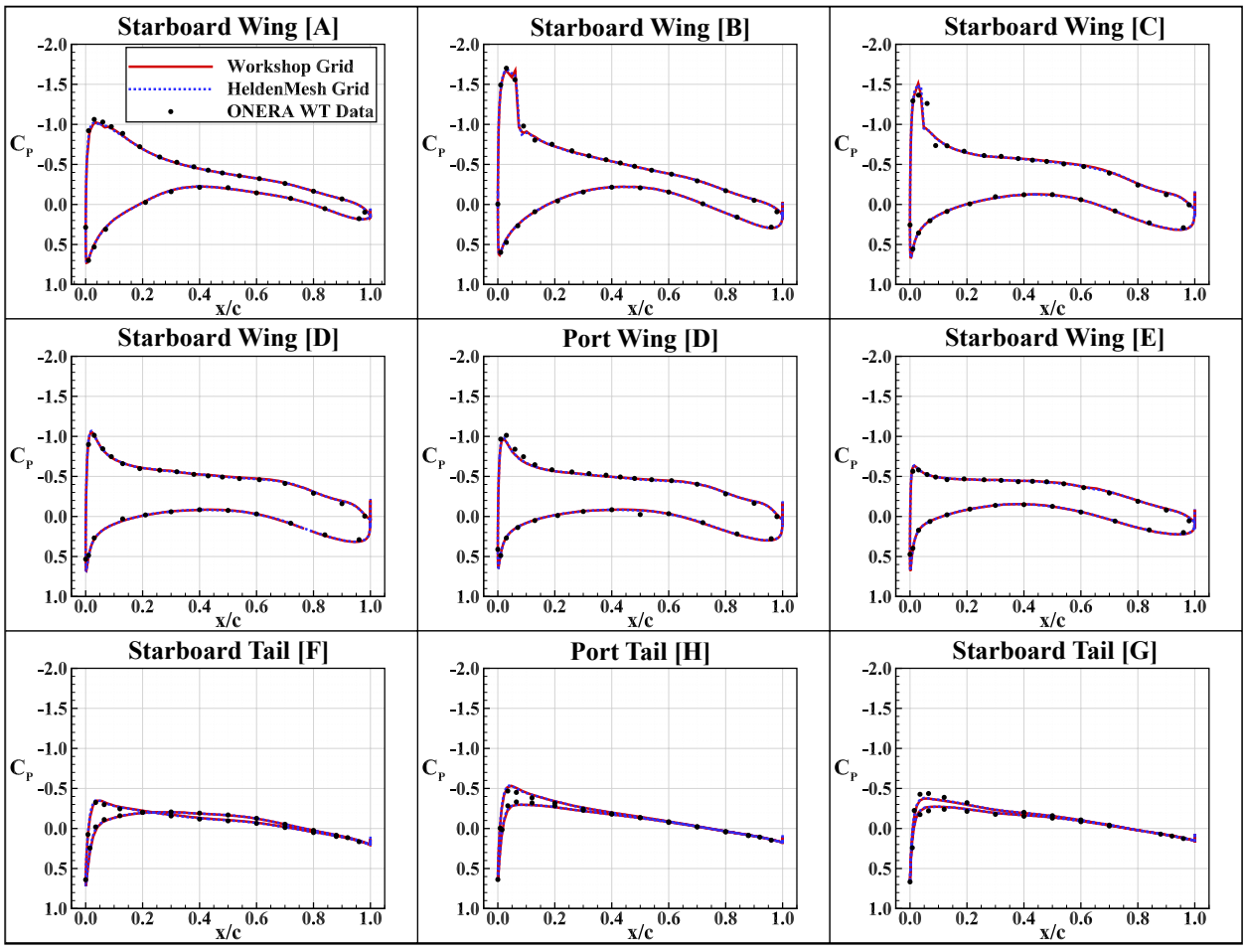

Figure 18. Sectional pressure distribution data at M = 0.70 (WT C_L = 0.510).

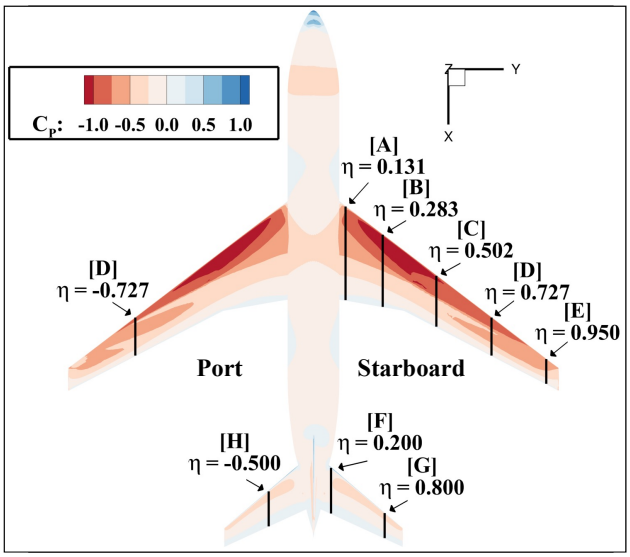

Figure 19. FUN3D pressure contours for medium refinement level of HeldenMesh™ grid at M = 0.83 (C_L = 0.5).

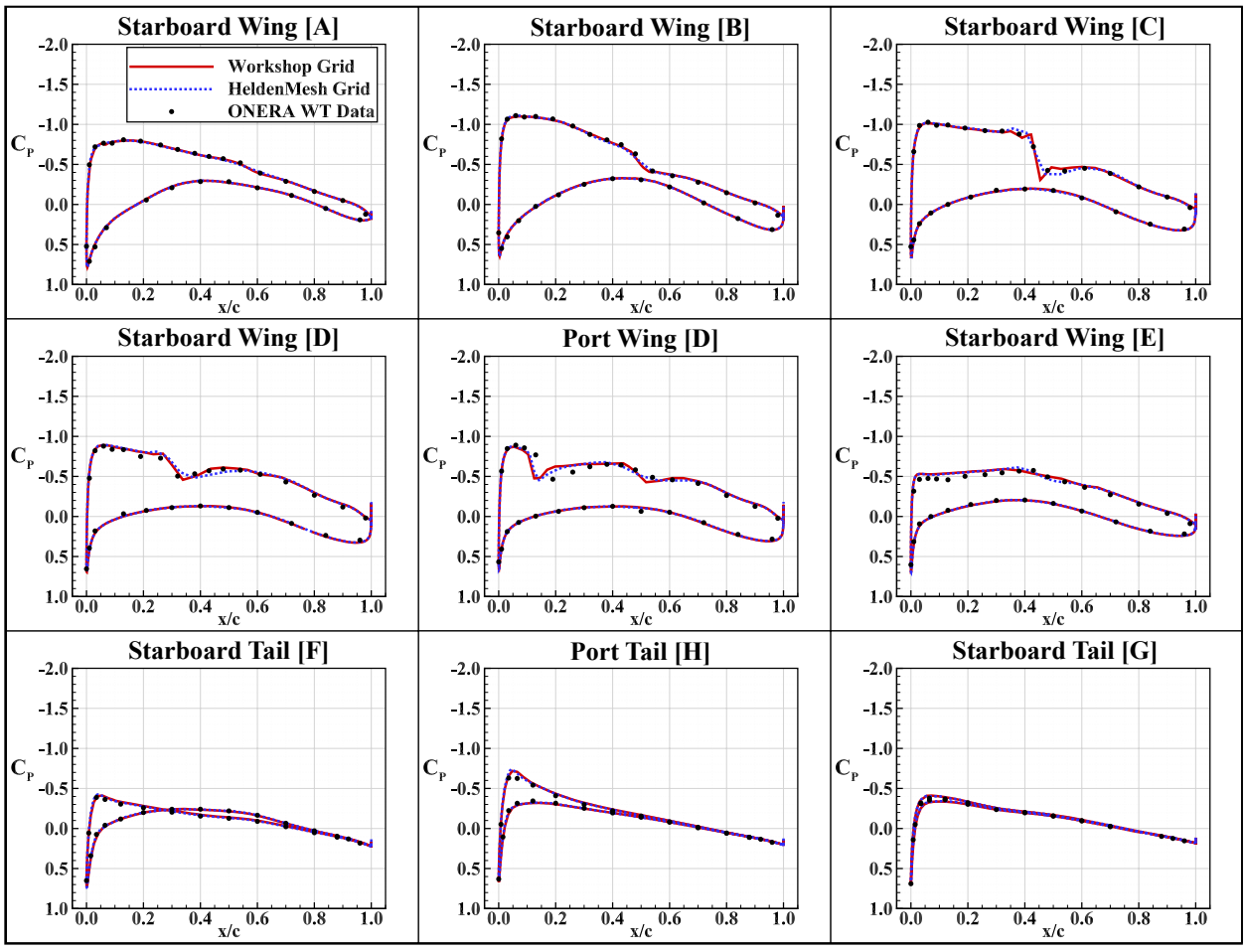

Figure 20. Sectional pressure distribution data at M = 0.83 (WT C_L = 0.510).

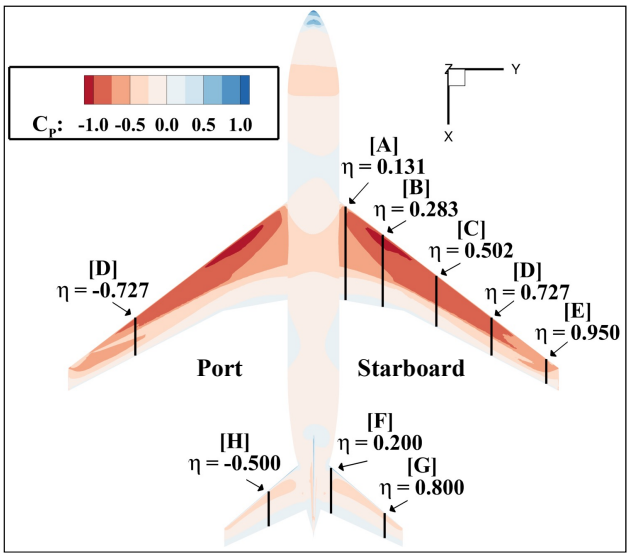

Figure 21. FUN3D pressure contours for medium refinement level of HeldenMesh™ grid at M = 0.85 (C_L = 0.5).

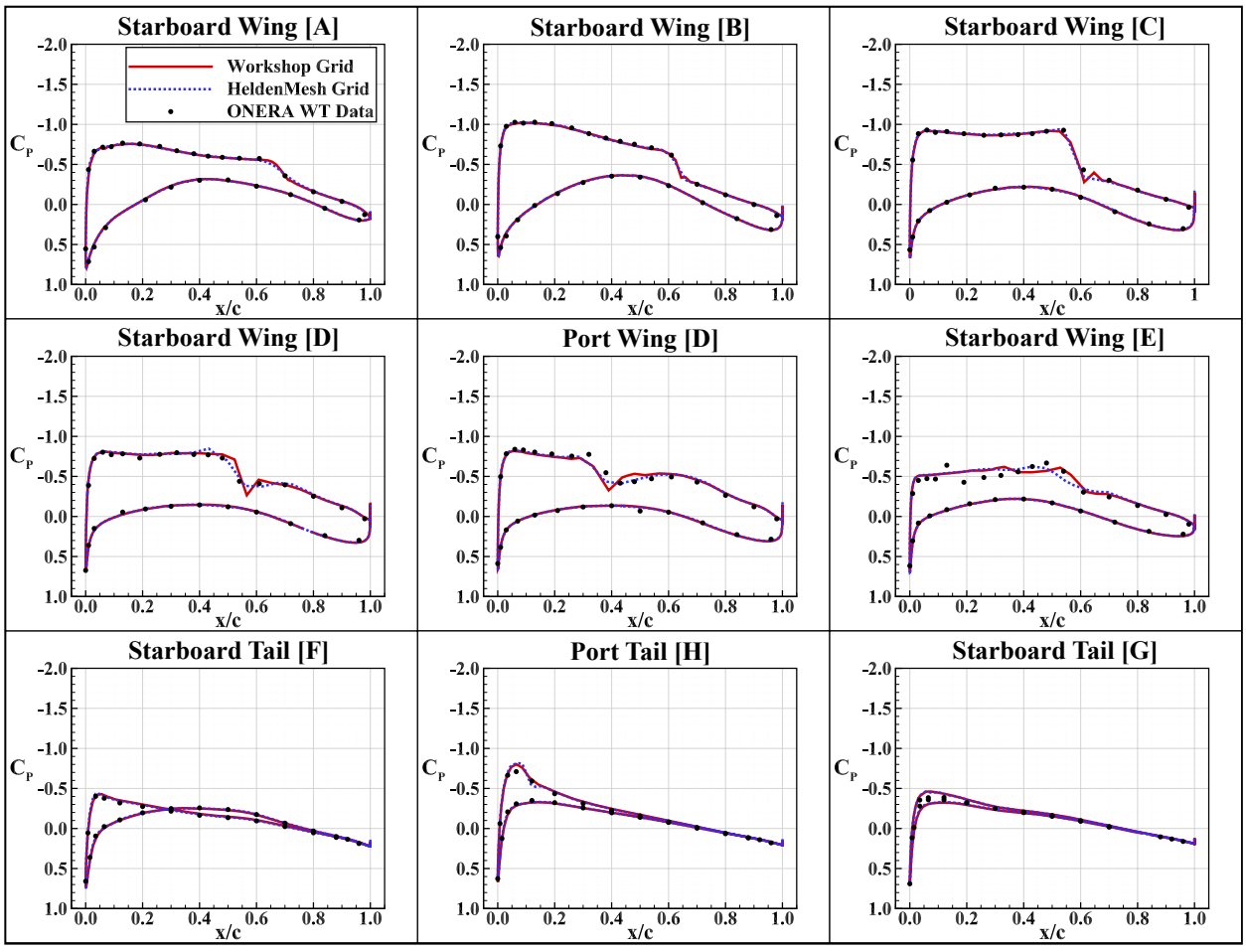

Figure 22. Sectional pressure distribution data at M = 0.85 (WT C_L = 0.510).

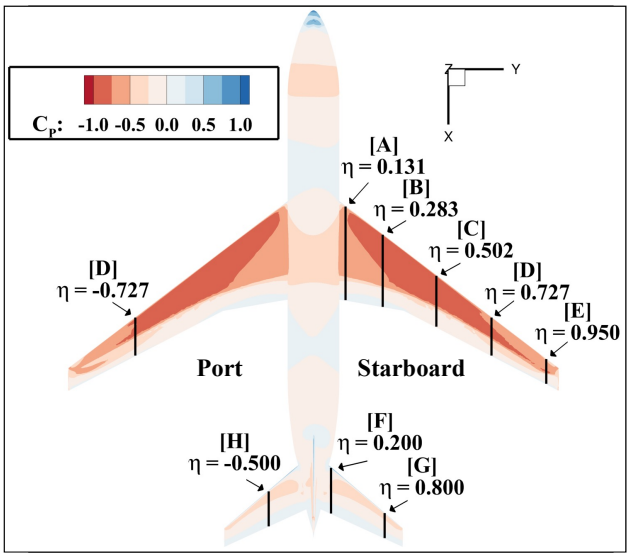

Figure 23. FUN3D pressure contours for medium refinement level of HeldenMesh™ grid at M = 0.87 (C_L = 0.5).

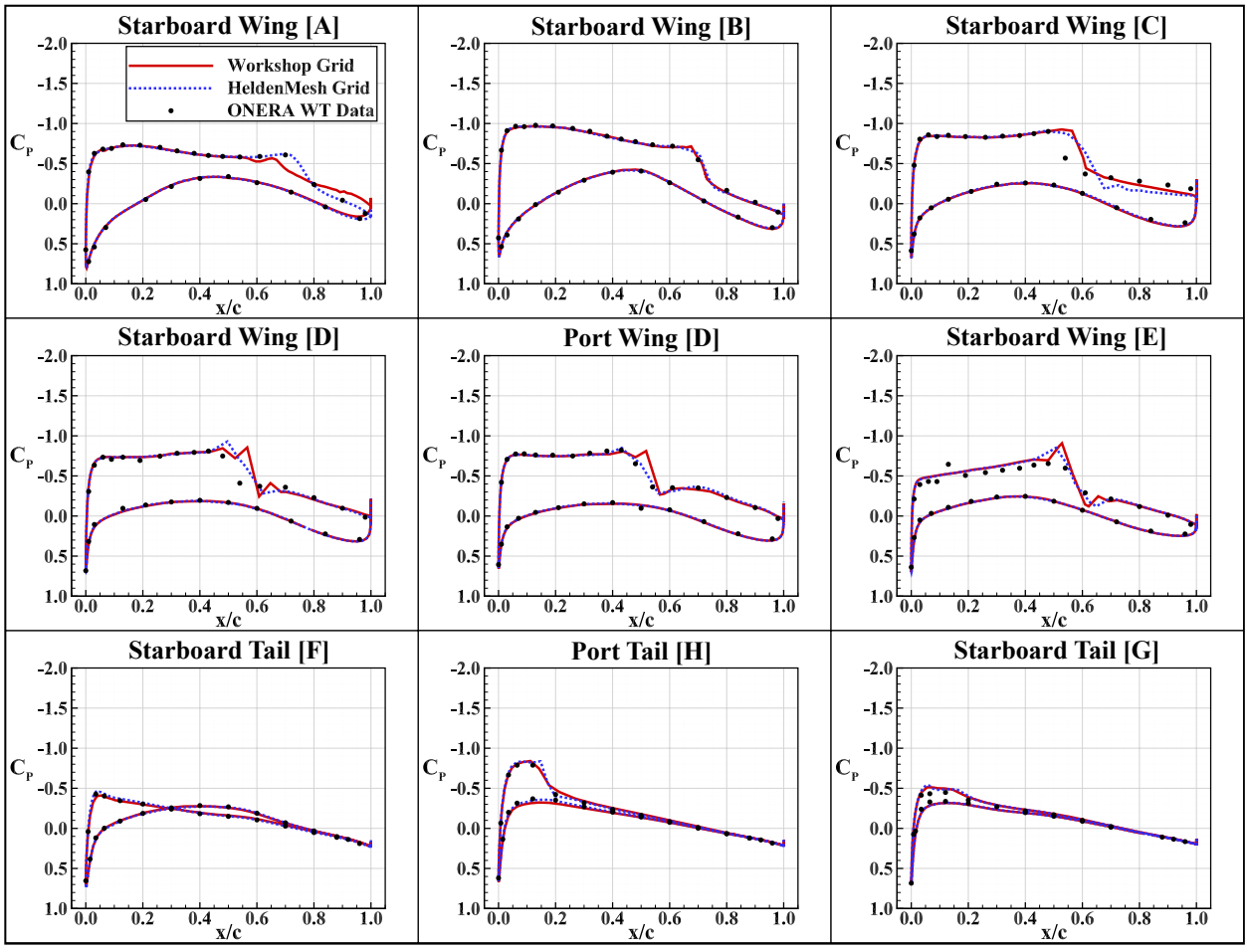

Figure 24. Sectional pressure distribution data at M = 0.87 (WT C_L = 0.510).

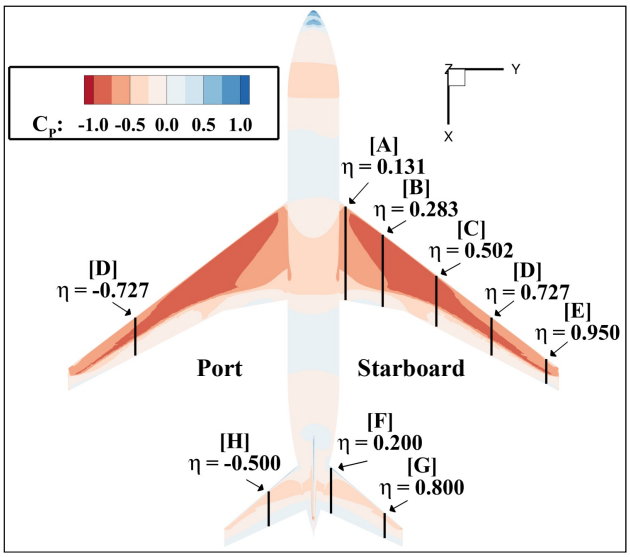

Figure 25. FUN3D pressure contours for medium refinement level of HeldenMesh™ grid at M = 0.90 (C_L = 0.5).

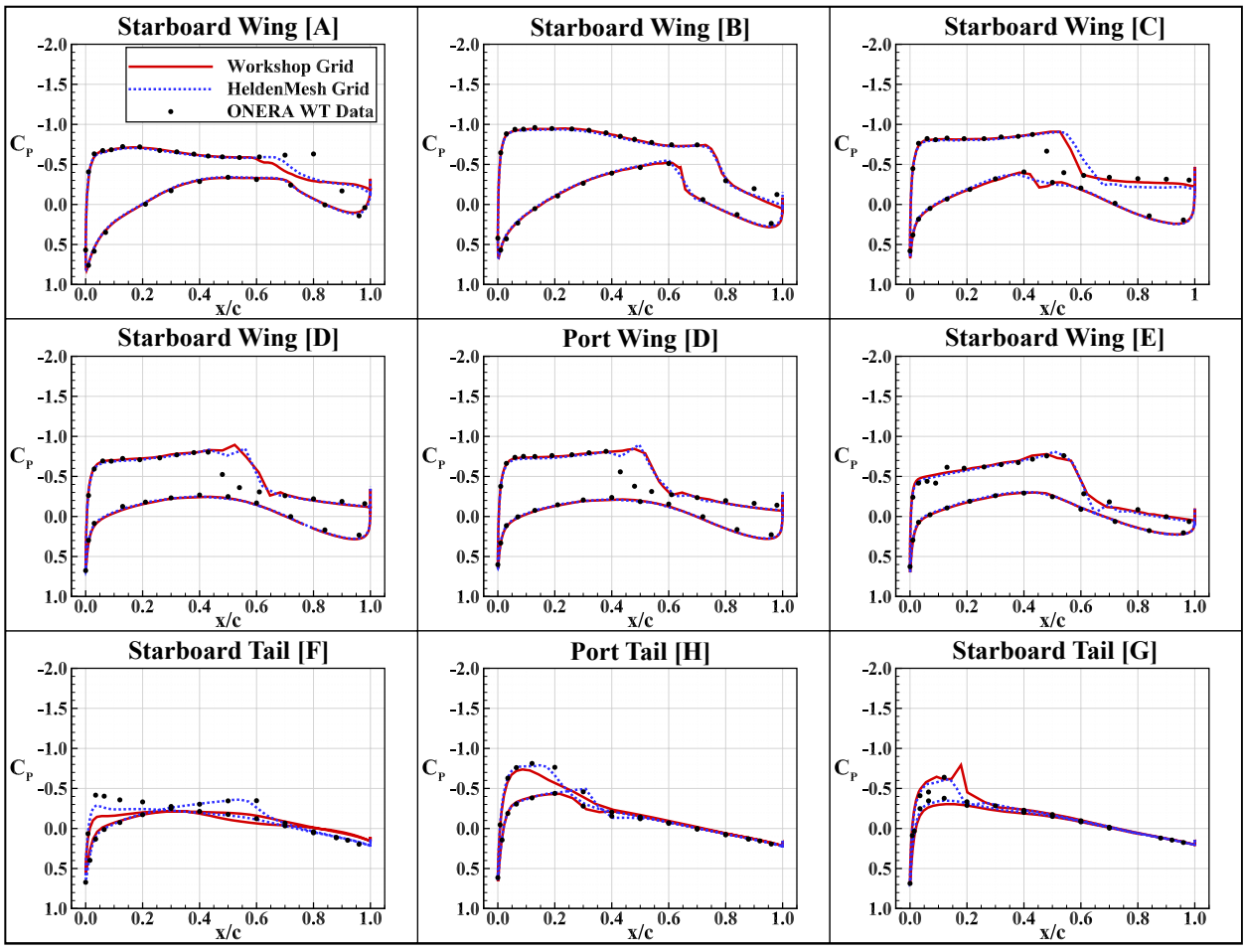

Figure 26. Sectional pressure distribution data at M = 0.90 (WT C_L = 0.510).

C. Case 4 - Wind Tunnel Sting Increments

Test case 4 was proposed to assess the static longitudinal stability increment due to the wind tunnel mounting sting for the LRM by calculating the differences in the force and moment coefficients for FUN3D simulations of the LRM configuration grids with and without the sting. The flow conditions correspond to $M = 0.83$ and $\beta = 1°$, where simulations were conducted for $C_L = 0.48$ and 0.52 so that an estimate in the pitching moment increment, $\Delta C_m/\Delta C_L$, at $C_L = 0.5$ could be calculated. All of the following results are presented in terms of sting-on minus sting-off increments using grids with the medium refinement.

Figure 27 shows the angle-of-attack and lift increments due to the sting for both the workshop and HeldenMesh™ grids. To maintain the target lift coefficients of 0.48 and 0.52, the results showed a range of 0.020 to 0.026 degrees of required increase in angle of attack for both grids. This increase in angle off attack leads to an increase in lift contribution from the fuselage and wings to compensate for a loss in lift from the tail component due to sting interference effects.

The increments in total and component drag coefficients due to the sting are shown in Fig. 28. Overall, the workshop and HeldenMesh™ grids show similar increments in each drag coefficient at the two lift conditions of interest. The total drag increment show a 6-count penalty due to the presence of the sting. On the component level, the sting acts to increase the drag contribution of the fuselage by 17 drag counts, while decreasing the drag contributions of the wings and tail, by approximately 2 and 7 drag counts, respectively.

Figure 29 provides the FUN3D predictions for sting increments in the total and component pitching moment coefficients. The static longitudinal stability increment is calculated as the slope of the line fit between the two data points. The workshop and HeldenMesh™ grids show a median stability increment of $\Delta C_m/\Delta C_L = 0.0119$ with the HeldenMesh™ grid increment being approximately 5% greater than that for the workshop grid. This increase in pitching moment increment for the HeldenMesh™ grid may be attributed to slightly higher increments on the wing and tail components, which were previously shown to have slight differences due to shock resolution. The magnitude of the pitching moment increments is greatest for the tail component, followed by the fuselage, with limited varation for the wings. This observation is not surprising given the proximity of the sting to the fuselage and tail components but is useful in quantifying the magnitude of the differences.

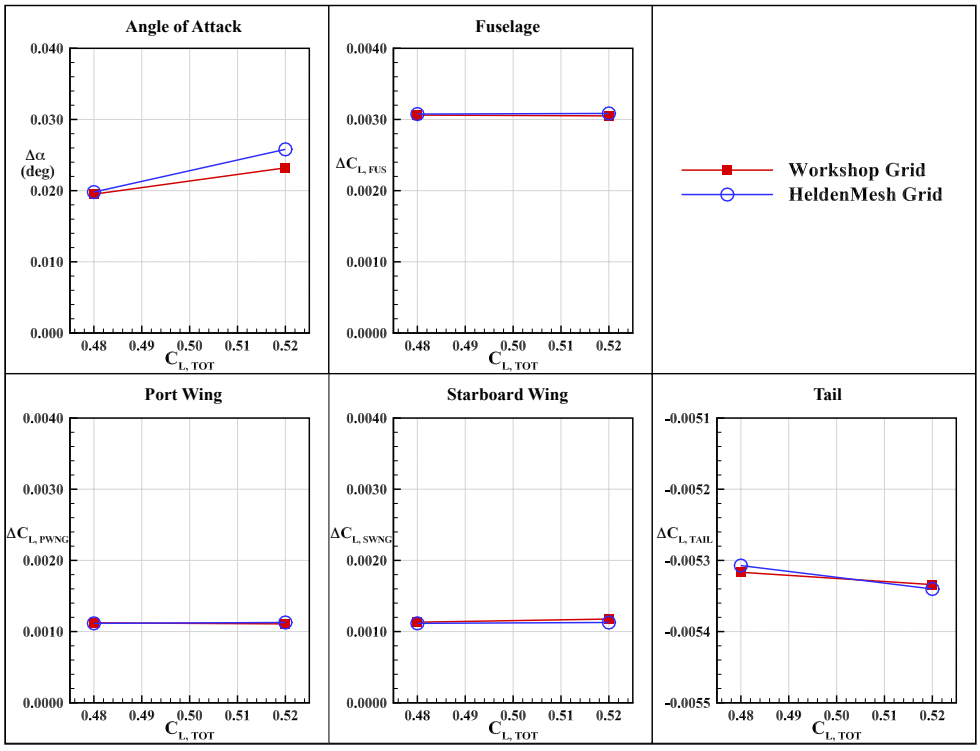

Figure 27. Increments in angle of attack and component lift coefficients due to the sting ($M = 0.83$, $C_L = 0.5$).

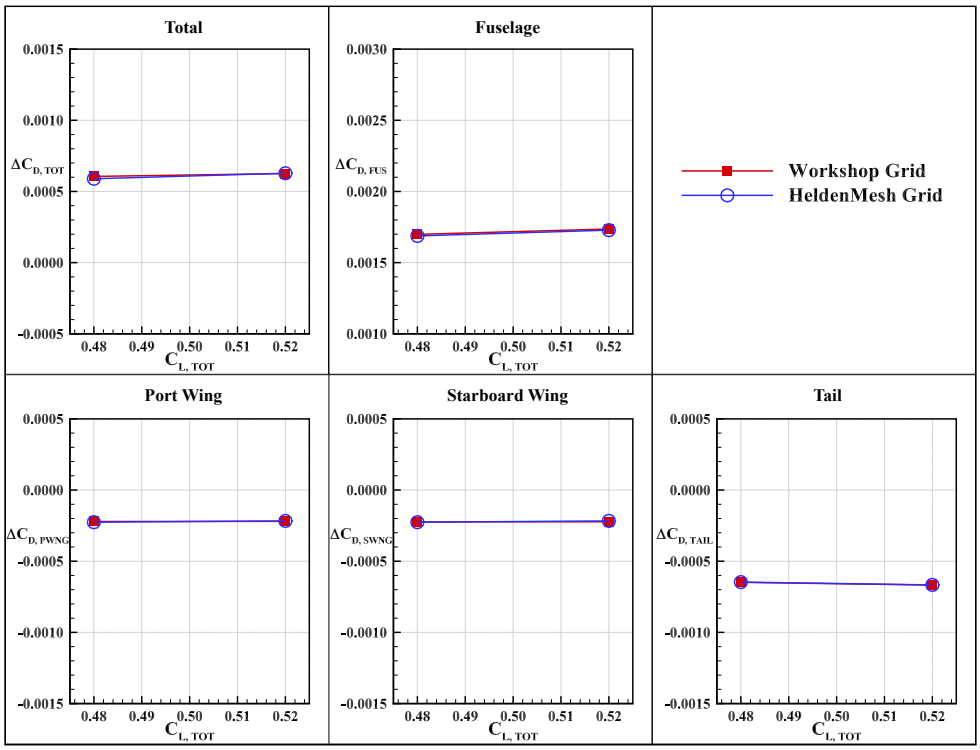

Figure 28. Increments in total and component drag coefficients due to the sting (M = 0.83, C_L = 0.5).

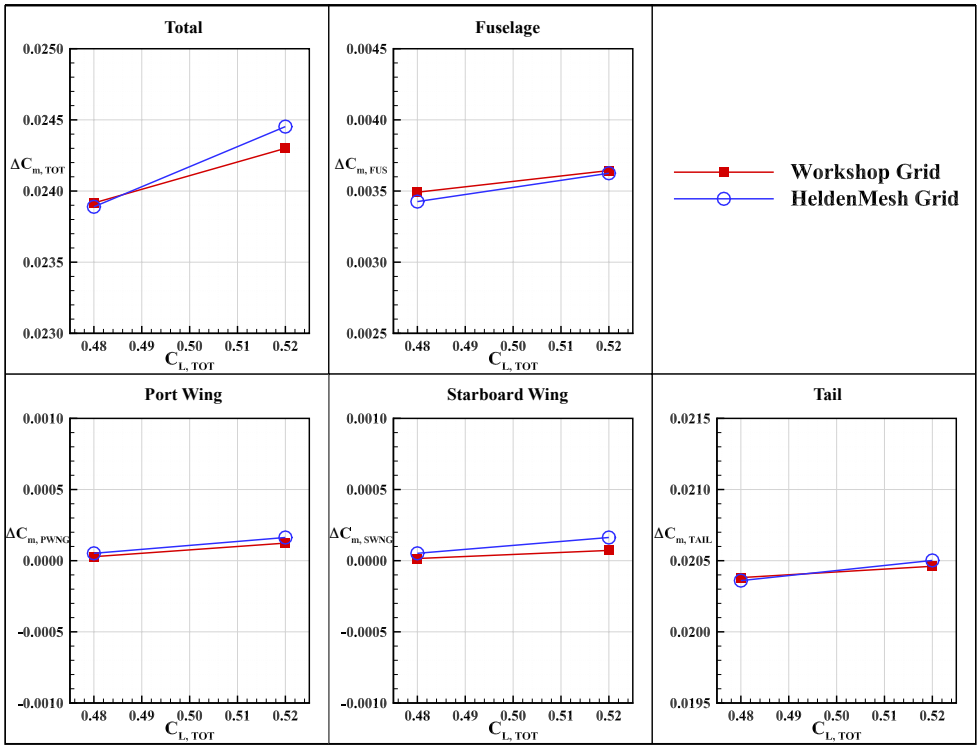

Figure 29. Increments in total and component pitching moment coefficients due to the sting (M = 0.83, C_L = 0.5).

D. Case 5 - Stability Derivative Calculation

Test case 5 was an optional case for participants who were asked to use their best practices to calculate the side force, rolling moment, and yawing moment derivatives at a zero sideslip angle with test case conditions corresponding to $\beta = 1°$, M = 0.83, and $C_L = 0.5 \pm 0.0001$. For the present work, the test case served as an opportunity to assess the impact of using volume-mirrored grids on lateral stability derivative predictions after observing an asymmetric volume in the workshop grids. These visual differences were illustrated previously in Fig. 3. Toward quantifying this impact, simulations were conducted at sideslip angles of $\beta = -1$ and $1°$. The lateral force and moment coefficient results at the unit sideslip angle provides an approximation for the lateral stability derivatives. For a symmetric configuration, one would expect that these derivative values be identical. Relative differences between these predicted derivative values can help assess their sensitivity to grid asymmetries for a "well-resolved" grid.

Figure 30 shows the total and component side force stability derivatives with respect to sideslip angle. The total sideforce stability derivative shows the success of the volume-mirrored HeldenMesh™ grids to predict the same value insensitive to sideslip orientation, whereas the workshop grids show a qualitative difference at positive and negative sideslip angles. However, it is important to note that these variations are on the order of a 0.0001 difference. The noted asymmetry observed in the workshop grid predictions may be attributed to differences between the tail and fuselage components. This trend is also observed for the lateral rolling and yawing moment derivatives, as seen in Figs. 31 and 32. These observations would suggest that the need for volume-mirrored grids may be diminished for grids with sufficient average spatial resolution throughout the domain of interest. In future workshops, this assumption should be revisited for any potential test cases involving highly maneuverable flight vehicles that may operate at extreme vehicle orientations at increased rates of speed, for which nonlinear and unsteady flow features become more significant.

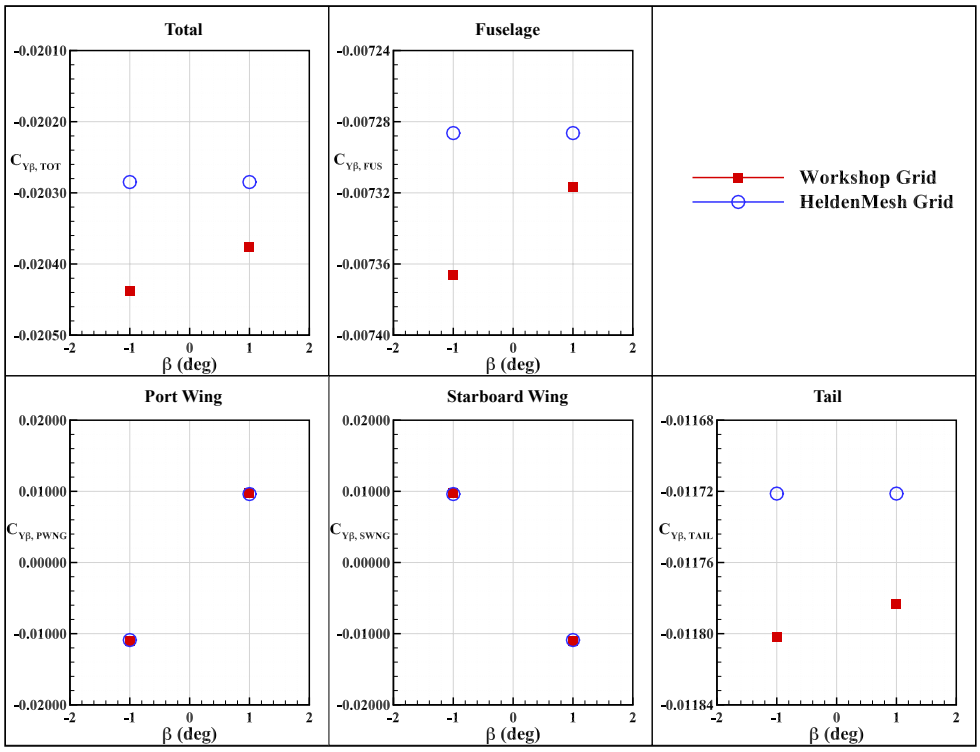

Figure 30. Side force stability derivative with respect to sideslip angle (M = 0.83, C_L = 0.5).

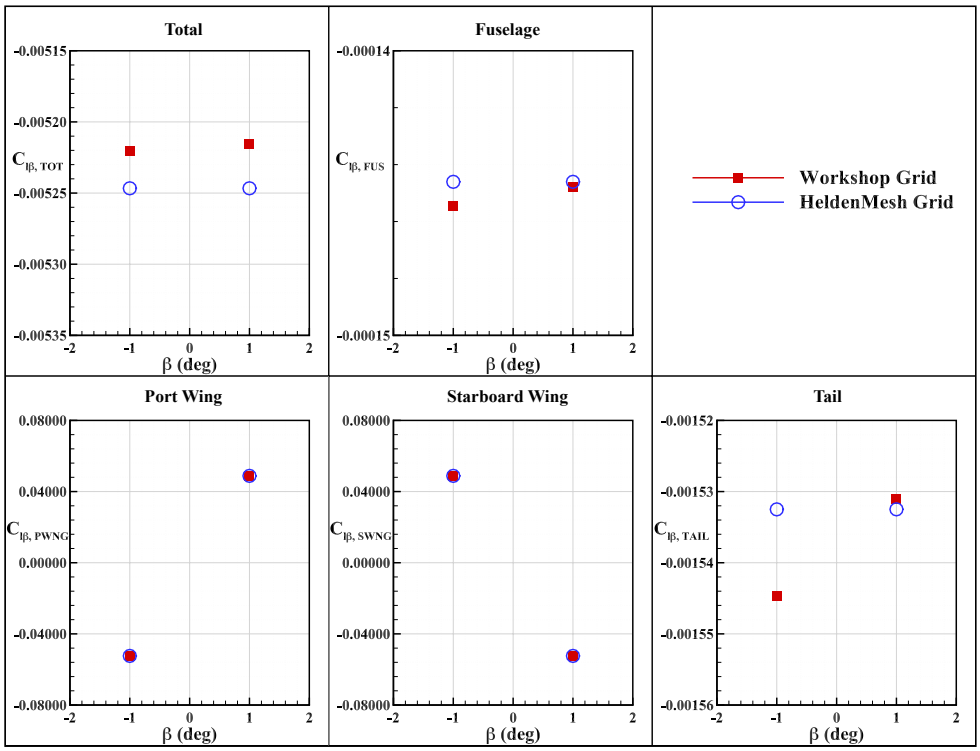

Figure 31. Rolling moment stability derivative with respect to sideslip angle (M = 0.83, C_L = 0.5).

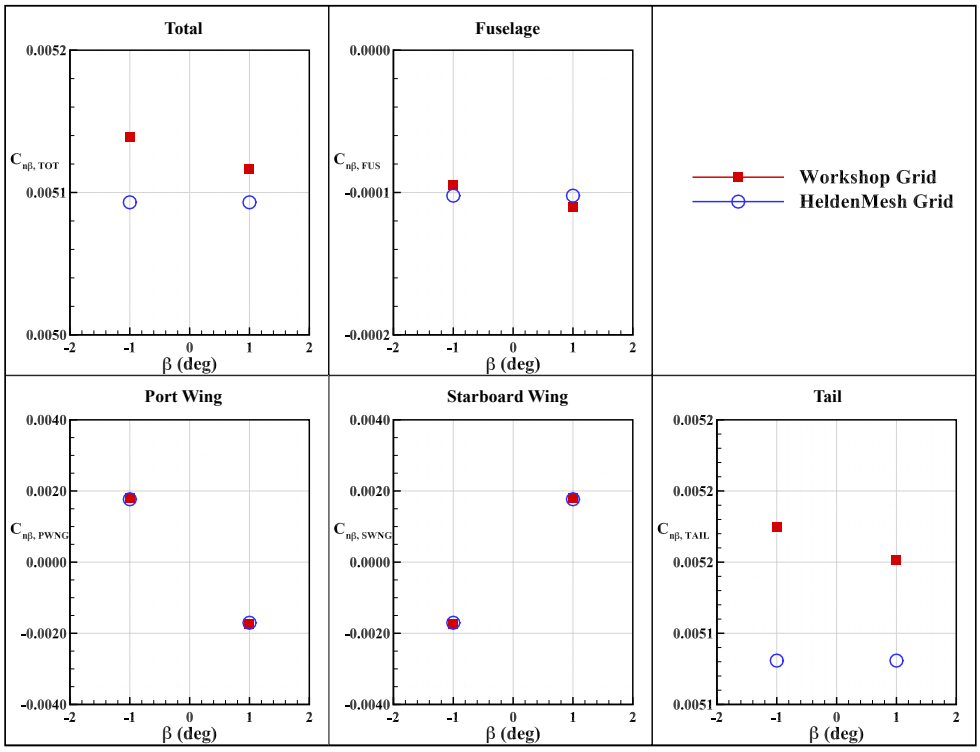

Figure 32. Yawing moment stability derivative with respect to sideslip angle (M = 0.83, C_L = 0.5).

E. Case 6 - Sideslip Angle Sweep

In Test Case 6, participants were asked to calculate the variations in predicted force and moment coefficients for a sideslip angle sweep that included $\beta = [1°, 3°, 5°]$ at $M = 0.83$ and $C_L = 0.5 \pm 0.0001$. Figure 33 shows the variation in total and component lift coefficients across the noted sideslip angle range. The total lift coefficient illustrates the succcess in each grid meeting the target lift coefficient at every sideslip angle with the exception of the workshop grid solution at $\beta = 5°$, which encountered issues in reaching a converged value with numerical stability. The component coefficients show that the grids agree favorably for the fuselage and starboard (more loaded) wing. Discrepancies between the grids arise for the port (less loaded) wing at the highest sideslip angle and for the tail component at every sideslip angle, with the HeldenMesh™ grid generally predicting a larger tail contribution relative to the workshop grid. This difference becomes more significant at the highest sideslip angle with nearly a 4-count difference in the tail lift contribution.

Figure 34 provides the FUN3D results for the total and component drag coefficients vs. sideslip angle. Both sets of grids show a decrease in drag coefficient by nearly 30 counts over the given sideslip angle range with differences most pronounced in the lower sideslip-angle range. The fuselage and wing components generally show limited variation between the grids while the results for the tail show a 5 to 10-count difference between the predictions. The side force coefficient results are shown in Fig. 35 and are observed to have a trend of linear decreases in total coefficient value with increased sideslip angles as the nose of the aircraft moves left. This linear variation may be attributed to differences in the fuselage and vertical tail components. For every coefficient, the workshop and HeldenMesh™ grids are in close agreement.

The total and component pitching moment coefficient variations with sideslip angle are shown in Fig. 36. The FUN3D solutions show a decrease in configuration pitching moment coefficient at larger sideslip angle values. The component coefficients show that the higher loaded, starboard wing and tail components contribute most to the decrease in total pitching moment coefficient. The HeldenMesh™ and workshop grids show the largest discrepancy at $\beta = 5°$, where HeldenMesh™ predicts a significantly smaller and negative pitching moment coefficient contribution from the tail relative to the workshop grids. The rolling and yawing moment results are shown in Figs. 37 and 38, respectively. Overall, the two sets of grids are in strong agreement for the total and component lateral moment coefficient values. The FUN3D solutions predict a nearly linear decrease in rolling moment and increase in yawing moment coefficient with increased sideslip angle.

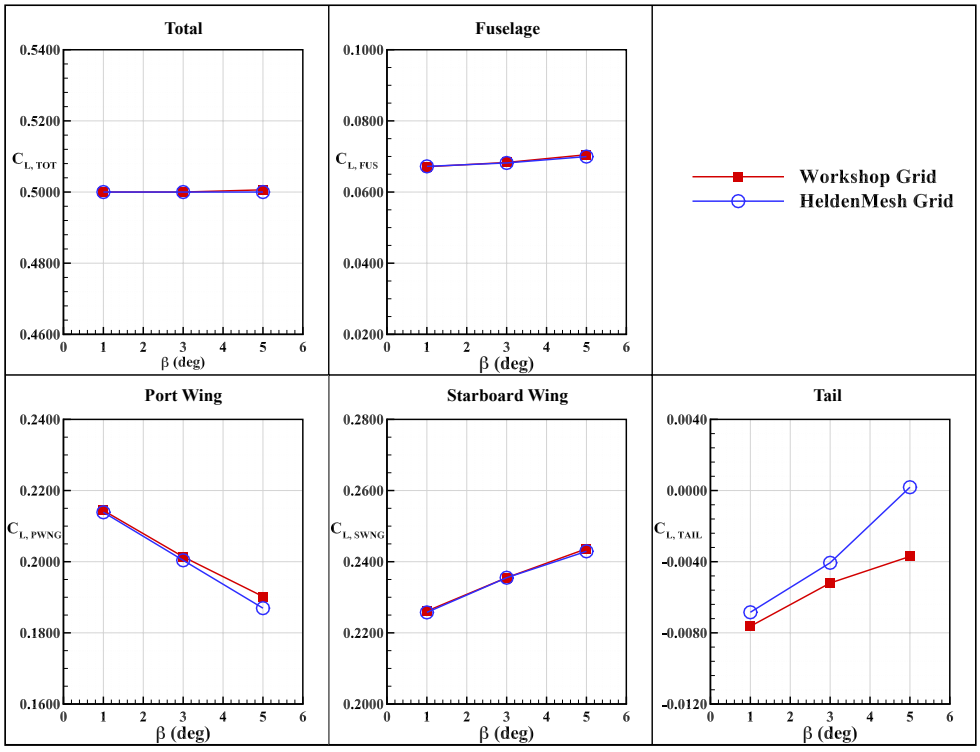

Figure 33. Total and component lift coefficients vs. sideslip angle (C_L = 0.5).

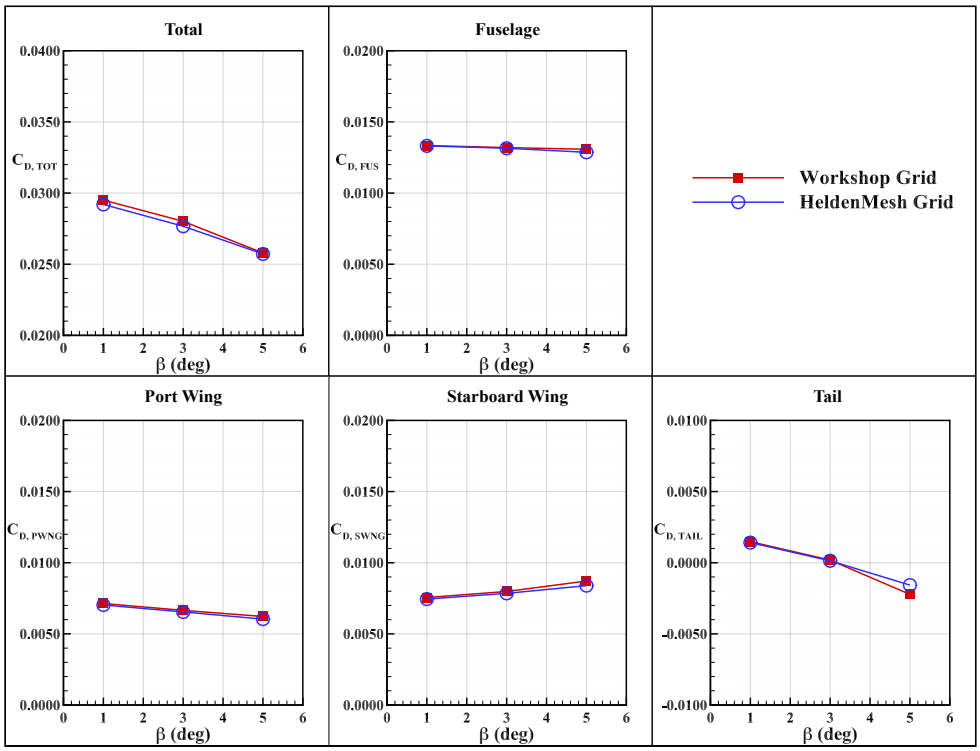

Figure 34. Total and component drag coefficients vs. sideslip angle (C_L = 0.5).

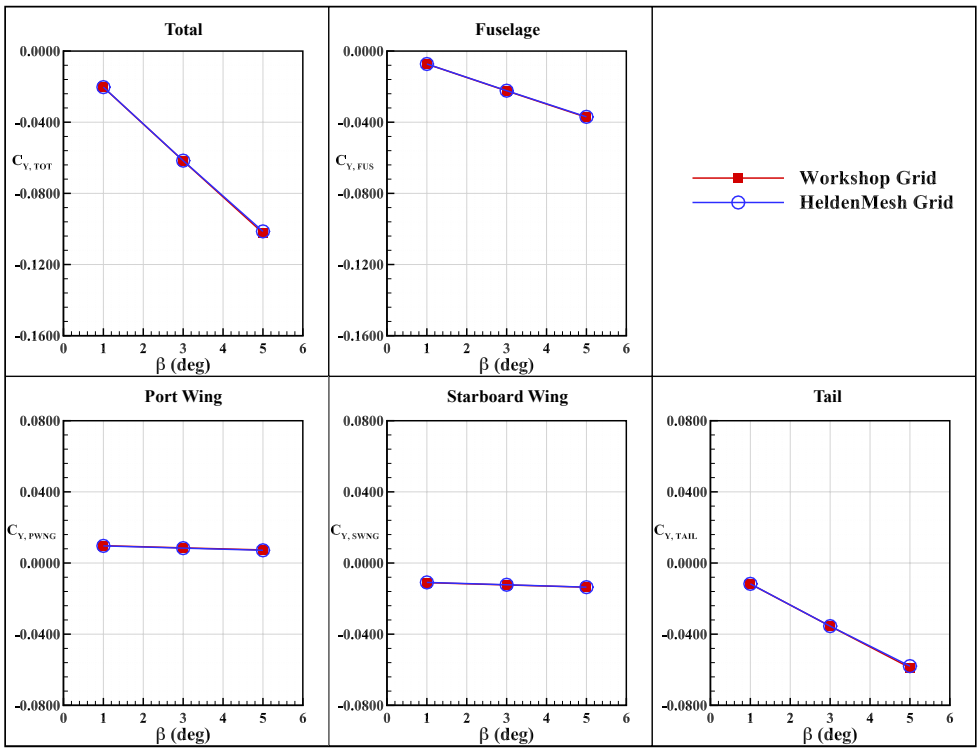

Figure 35. Total and component side force coefficients vs. sideslip angle (C_L = 0.5).

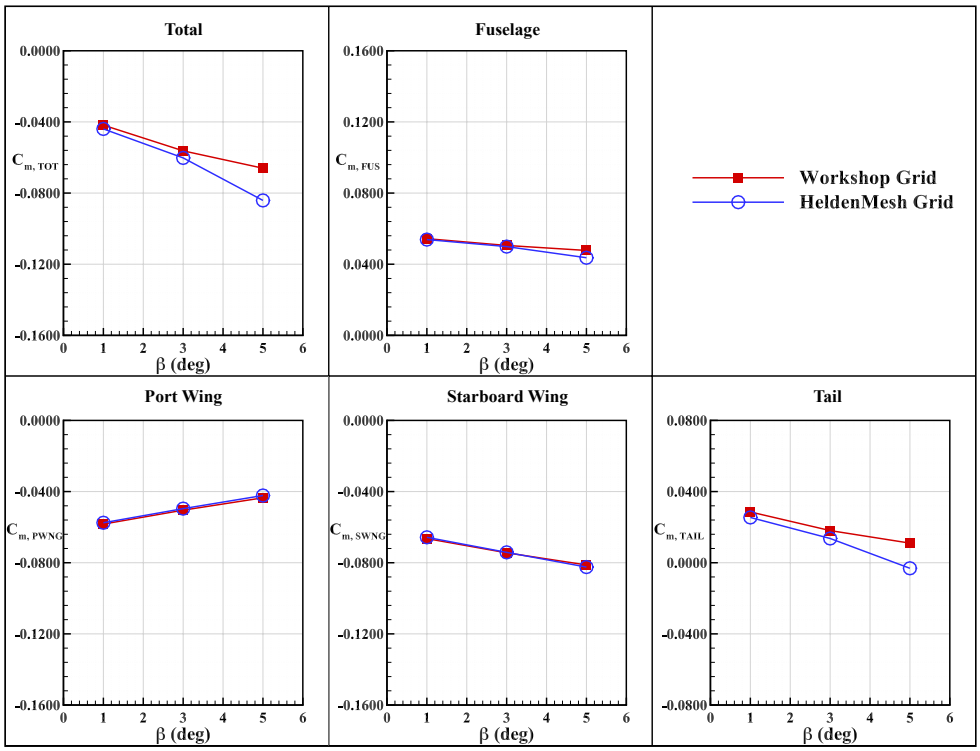

Figure 36. Total and component pitching moment coefficients vs. sideslip angle (C_L = 0.5).

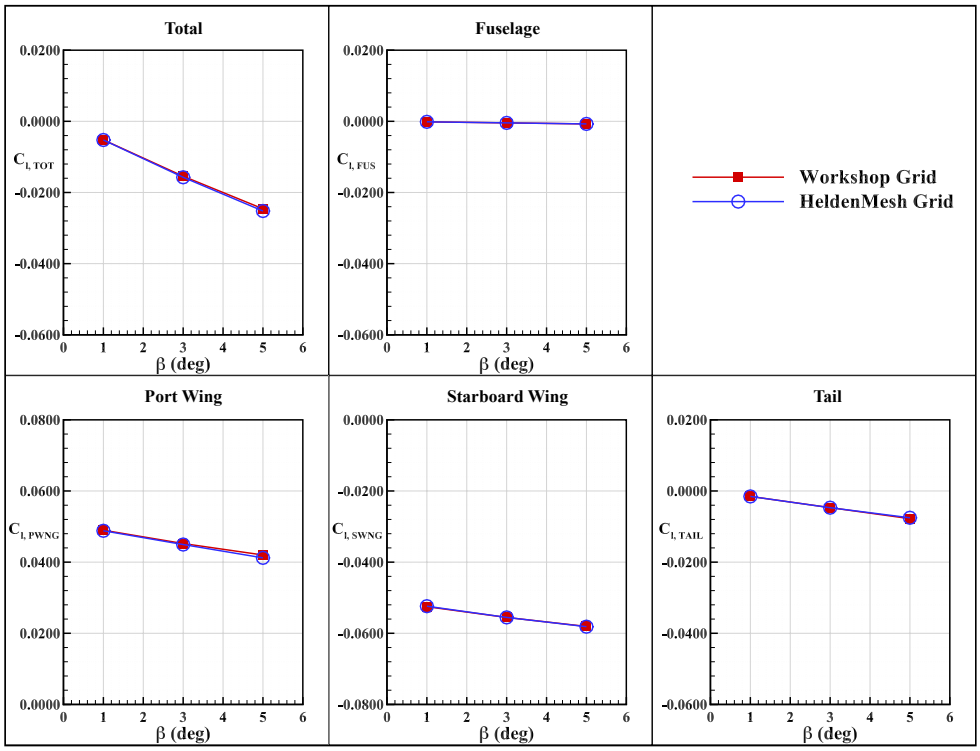

Figure 37. Total and component rolling moment coefficients vs. sideslip angle (C_L = 0.5).

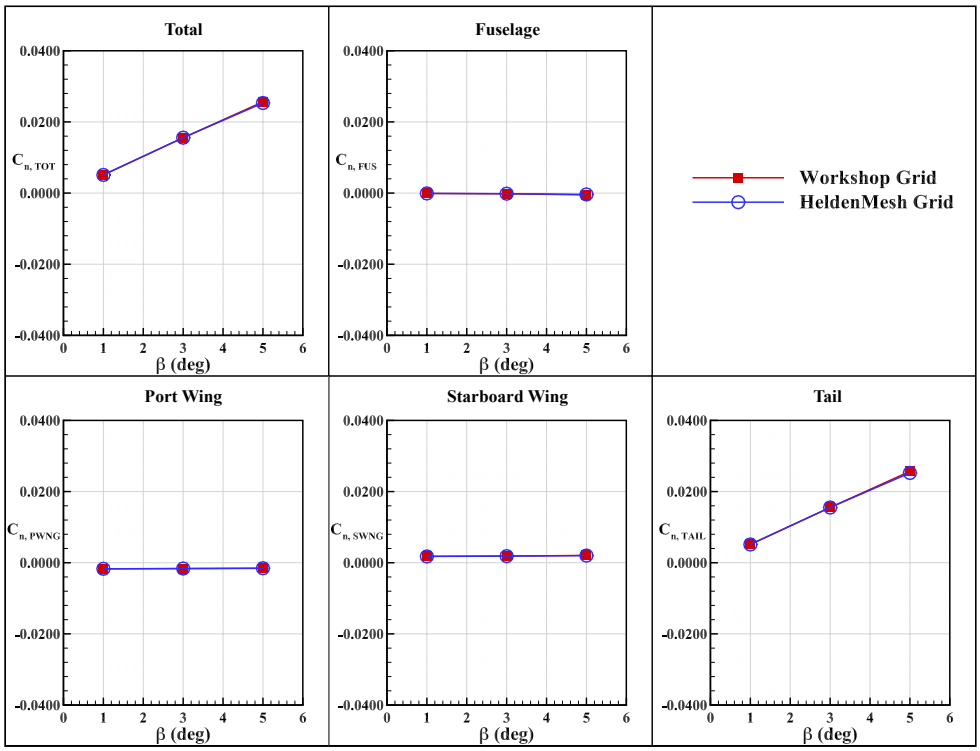

Figure 38. Total and component yawing moment coefficients vs. sideslip angle (C_L = 0.5).

VI. Conclusions

NASA FUN3D flow solver results for the 1st AIAA Stability and Control workshop are presented on behalf of participants from the NASA Langley Research Center. Results were generated for two series of unstructured, mixed-element grids, one set provided by the workshop and another set created using the HeldenMesh™ grid generation software. These additional grids were generated in part due to the authors' familiarity with the software but also to investigate the impact of volume-mirrored grids on lateral stability derivative predictions. Steady-state numerical simulations were conducted for the following workshop test cases: a grid convergence study, investigation of the Mach number effect on static stability, quantification of wind tunnel sting increments, an optional case on static lateral stability-derivatives, and a sideslip angle sweep.

The grid convergence study showed reasonable agreement between the experimental data and computational results for each aerodynamic force and moment coefficient with the exception of pitching moment. The FUN3D solutions for both the workshop and HeldenMesh™ grids predicted a significantly more negative pitching moment by approximately 20%. The component breakdown of pitching moment showed that the horizontal and vertical tail components had the largest impact on this variability in pitching moment. The inability to predict pitching moment remains one of the more challenging aerodynamic quantites to predict using RANS-based solvers for S&C predictions. In terms of grid convergence, the HeldenMesh™ grid series showed a relatively linear solution fit for each aerodynamic coefficient, whereas the workshop grids illustrated a more nonlinear variation. In any case, the medium refinement level was determined to be sufficient for comparisons to wind tunnel data based on the agreement in magnitude with the experimental force and moment measurements.

The FUN3D results for the Mach number sweep showed favorable agreement in predicting the drag rise up to M = 0.90, where both the workshop and HeldenMesh™ grids underpredicted the total drag coefficient by an average of 50 drag counts. The side force coefficient predictions showed qualitative agreement with experimental data up to M = 0.85 but overpredicted the total coefficient by approximately 10%. Beyond M = 0.85, there was notable scatter in trend and magnitude for the FUN3D predictions. The grid-to-grid variability in side force predictions were shown to be attributed to the fuselage and tail components. The pitching moment coefficient results continued to predict a more negative pitching moment coefficient by approximately 10% in the lower Mach number range. While not lift-matched within the desired tolerance, the workshop grid showed excellent agreement with wind tunnel data at M = 0.87 and 0.90,

predicting a sharp increase in pitching moment, i.e., loss of aft vehicle loading. The HeldenMesh™ grid showed an abrupt increase in pitching moment coefficient, which looked to be attributed to the tail component. Pressure distribution data comparisons along the wing and horizontal tail components at $M = 0.90$ were fairly consistent between the grids and wind tunnel data, suggesting that the tail variability may be a result of prediction differences on the vertical tail. In the case of rolling moment coefficient, the FUN3D solutions showed excellent agreement with the wind tunnel data and between each other with slight differences in the predicted wing contributions to rolling moment. The results for yawing moment coefficient seemed to provide a reasonable qualitative match with wind tunnel data from $M = 0.70$ to 0.85 with a slight underprediction of the coefficient by up to 5%. Similar to pitching moment, these differences could be primarily attributed to the tail. Overall, the results of the Mach sweep study suggest that reasonable aerodynamic predictions could generally be obtained with most difficulties encountered in predicting the pitching moment and sideforce coefficient. Future studies may benefit from grid convergence and/or adaptation studies at the higher Mach numbers to better resolve the shock features on the wing and tail components.

The wind tunnel sting increment test case showed an average increase in drag coefficient by approximately 6 counts with the most significant component increment being the fuselage. The pitching moment increment ranged from 0.0239 at $C_L = 0.48$ to 0.0245 at $C_L = 0.52$. The tail component had the largest impact on the pitching moment coefficient, followed by the fuselage, which is intuitive given their proximity to the wind tunnel mounting sting. The workshop and HeldenMesh™ grids showed a median stability increment of $\Delta C_m/\Delta C_L = 0.0119$ with the HeldenMesh™ grid increment being approximately 5% greater than that for the workshop grid. The component increments suggest that this is due to slighty greater predictions of the wing and tail contributions to pitching moment increment.

The optional test case for calculating static stability derivatives was used as an opportunity to assess the impact of volume-mirrored grids on lateral stability derivative coefficients. Simulations were conducted at $\beta = -1^\circ$ and 1° for the medium refinement levels of the workshop and HeldenMesh™ grids, for which the lateral coefficients represent the lateral stability derivatives with respect to sideslip angle. For a symmetric configuration, one would expect these derivative values to show minimal differences at small sideslip angles. The FUN3D results were able to confirm the propagation of grid asymmetry to the lateral stability derivatives for the workshop grids; however, the differences were typically less than 1 count and would have limited impact on computational S&C predictions in consideration of typical CFD uncertainties. Future workshops may revisit this assumption in the case of dynamic S&C predictions that may include highly maneuverable vehicles operating within nonlinear angle-of-attack and sideslip angle ranges at high rates of motion.

The final test case focused on generating FUN3D solutions across a sideslip angle range of $\beta = 1^\circ$ to 5°. Overall, both the workshop and HeldenMesh™ grids showed strong consistency in the total and component force and moment coefficients. The most notable discrepancies arose in the total pitching moment coefficient, especially at the highest sideslip angle, for which a nonlinear variation in the coefficient is observed. The differences between the two solutions was attributed to differences in the pitching moment contribution from the horizontal and vertical tail components. Future workshops may consider exploring the impact of wake sources near the wing and tail components to better assess its importance on aerodynamic predictions at relatively large sideslip angles.

VII. Acknowledgements

The authors would like to acknowledge the 1st AIAA Stability and Control Prediction Workshop committee members for their efforts in organizing and conducting a succesful, inaugural workshop. Additionally, special thanks to Carolyn Woeber and Kristen Shoemake of Pointwise Inc., who developed the set of unstructured grids for the ONERA LRM configuration.

References

[1] Tinoco, E. N., Brodersen, O. P., Keye, S., Laflin, K. R., Feltrop, E., Vassberg, J. C., Mani, M., Rider, B., Wahls, R. A., Morrison, J. H., et al., "Summary Data from the Sixth AIAA CFD Drag Prediction Workshop: CRM cases," *Journal of Aircraft*, Vol. 55, No. 4, 2018, pp. 1352–1379.

[2] Vassberg, J., Dehaan, M., Rivers, M., and Wahls, R., "Development of a Common Research Model for Applied CFD Validation Studies," *26th AIAA Applied Aerodynamics Conference*, 2008, p. 6919.

[3] Cartieri, A., Hue, D., Chanzy, Q., and Atinault, O., "Experimental Investigations on Common Research Model at ONERA-S1MA–Drag Prediction Workshop Numerical Results," *Journal of Aircraft*, Vol. 55, No. 4, 2018, pp. 1491–1508.

[4] Corporation, H. A., "HeldenMesh User Manual, Version 3.02," 2018.

[5] Biedron, R. T., Carlson, J.-R., Derlaga, J. M., Gnoffo, P. A., Hammond, D. P., Jones, W. T., Kleb, B., Lee-Rausch, E. M., Nielsen, E. J., Park, M. A., et al., "FUN3D Manual: 13.6," 2019.

[6] Vassberg, J. C., Tinoco, E. N., Mani, M., Rider, B., Zickuhr, T., Levy, D. W., Brodersen, O. P., Eisfeld, B., Crippa, S., Wahls, R. A., et al., "Summary of the Fourth AIAA Computational Fluid Dynamics Drag Prediction Workshop," *Journal of Aircraft*, Vol. 51, No. 4, 2014, pp. 1070–1089.

[7] Chyczewski, T., Lofthouse, A., Gea, L.-M., Cartieri, A., and Hiller, B., "Summary of the First AIAA Stability and Control Prediction Workshop," *AIAA SciTech 2022 Forum*, 2022.

[8] Frink, N. T., Pirzadeh, S. Z., Parikh, P. C., Pandya, M. J., and Bhat, M., "The NASA Tetrahedral Unstructured Software System (TetrUSS)," *The Aeronautical Journal*, Vol. 104, No. 1040, 2000, pp. 491–499.

[9] Allmaras, S. R., and Johnson, F. T., "Modifications and Clarifications for the Implementation of the Spalart-Allmaras Turbulence Model," *Seventh International Conference on Computational Fluid Dynamics (ICCFD7)*, Vol. 1902, Big Island, HI, 2012.

[10] Shur, M. L., Strelets, M. K., Travin, A. K., and Spalart, P. R., "Turbulence Modeling in Rotating and Curved Channels: Assessing the Spalart-Shur Correction," *AIAA Journal*, Vol. 38, No. 5, 2000, pp. 784–792.

[11] Spalart, P. R., "Strategies for Turbulence Modelling and Simulations," *International Journal of Heat and Fluid Flow*, Vol. 21, No. 3, 2000, pp. 252–263.

[12] Roe, P. L., "Approximate Riemann solvers, Parameter vectors, and Difference Schemes," *Journal of Computational Physics*, Vol. 43, No. 2, 1981, pp. 357–372.

[13] Roache, P. J., and Knupp, P. M., "Completed Richardson Extrapolation," *Communications in Numerical Methods in Engineering*, Vol. 9, No. 5, 1993, pp. 365–374.